Published in *Tribology Letters*
The final publication is available at Springer via
http://dx.doi.org/10.1007/s11249-017-0818-8

Design-driven modeling of surface-textured full-film lubricated sliding: validation and rationale of non-standard thrust observations

Jonathon K. Schuh[1], Yong Hoon Lee[1],
James T. Allison[2], Randy H. Ewoldt[1]*

[1]*Department of Mechanical Science and Engineering*
University of Illinois at Urbana-Champaign, Urbana, Illinois 61801
[2]*Department of Industrial Enterprise and Systems Engineering*
University of Illinois at Urbana-Champaign, Urbana, Illinois 61801

Abstract: Our recent experimental work showed that asymmetry is needed for surface textures to decrease friction in full-film lubricated sliding (e.g. thrust bearings) with Newtonian fluids; textures reduce the shear load and produce a separating normal force [1]. However, standard slider bearing theory cannot explain the sign of the observed normal thrust, and any effort to optimize surface textures would be premature if modeling and simulations are not validated with experiments. Here we model the flow with the Reynolds equation in cylindrical coordinates, numerically implemented with a pseudo-spectral method. The model predictions match experiments, rationalize the sign of the normal force, and allow for design of surface texture geometry. To minimize sliding friction with angled cylindrical textures, an optimal angle of asymmetry β exists. The optimal angle depends on the film thickness but not the sliding velocity within the applicable range of the model. Outside the scope of this paper, the model is being used to optimize generalized surface texture topography [2].

Key words: Surface textures, Reynolds equation, Pseudo-spectral method, Optimization

*Corresponding author: Email: ewoldt@illinois.edu, Phone: +1 (217) 333-6532

1. Introduction

We have previously shown experimentally (setup shown in Figure 1) that asymmetry is required to reduce friction in full film lubrication by reducing the apparent shear stress and by producing a separating normal force between the two surfaces [1, 3]. There, we minimized experimental effects (inertia, gap accuracy, non-parallelism, and surface tension) in order to obtain accurate results with gap-controlled bi-directional sliding conditions, and the normal forces were attributed to viscous effects up to gap based Reynolds number $\mathrm{Re}_h \equiv \frac{\rho \Omega R h}{\eta} = 1.21$. We choose this data set for validating a design-driven model because it involves asymmetric depth profiles (slanted-bottom circular texture) with the most complete data set including bi-directional sliding, shear and normal load measurement, controlled gap conditions, and precisely known texturing profiles. Shen and Khonsari [4] performed similar experiments with millimetric sized textures, but they focused on single directional sliding with cavitation effects. The data set that we obtained is simpler, because cavitation effects are not included.

Previous numerical studies with asymmetric surface textures [5, 6] are unable to correctly capture the sign of the experimental normal forces (Figure 2). Traditional slider bearing theory (where the pressure is set equal to zero at the periodic boundaries of the texture) is also unable to correctly capture the sign of the normal force [7]. Our experiments show that a positive normal force is generated with a *diverging* wedge, i.e. as if a standard slider bearing were operated in the reverse direction, which is not predicted by previous studies [5, 6, 7]. Given those *non-trivial* experimental results, here we wish to (i) determine a theoretical understanding for the velocity-dependent sign of the observed normal force, and (ii) validate a mathematical model that can be

used for design optimization of the surface textures (i.e. a design-driven model). Without the validation performed here, any optimization efforts would be premature.

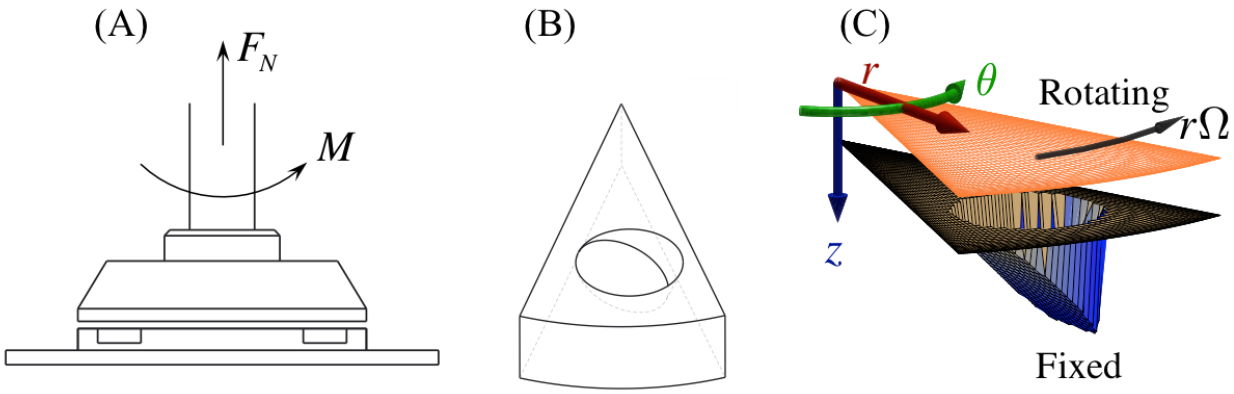

Figure 1: Experimental and numerical setup. (A) experimental setup previously used [1]; lower disk textured with ten periodic regions, each with an identical circular texture. (B) experimental periodic texture cell. Simulations involved one periodic textured cell. (C) simulated periodic texture with top flat plate moving in the direction of positive angular velocity (note: z axis stretched compared to r).

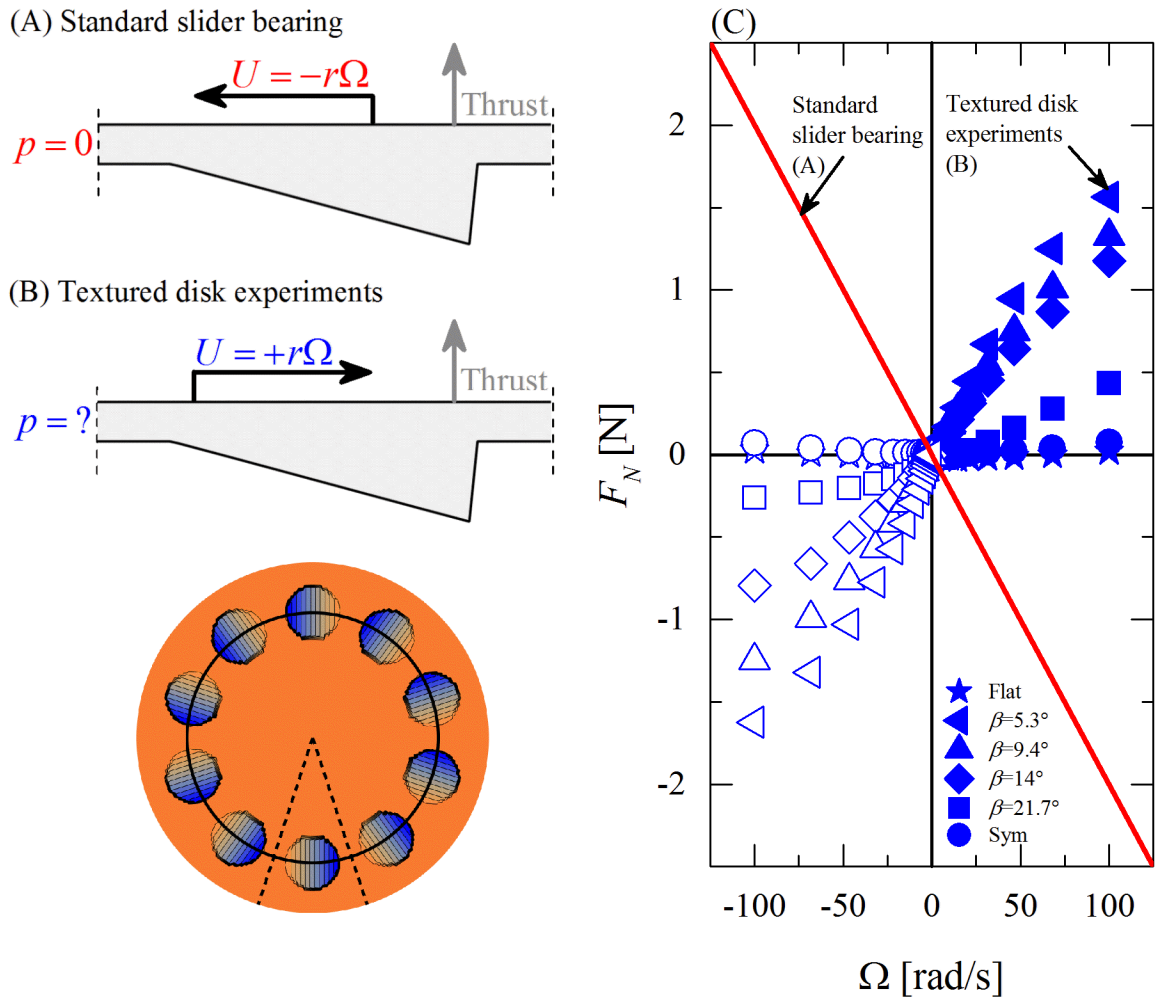

Figure 2: Standard slider bearing theory cannot predict the generated thrust in the textured disk experiments of Schuh and Ewoldt [1]. (A) standard slider bearing, pressure is zero at periodic boundaries. (B) textured disk experiments, pressure at periodic boundaries is not explicitly controlled; centerline of a single periodic texture and full textured disk are shown. (C) comparison of experimental normal force at h_0=269 μm [1, 3] to a standard slider bearing. The experiments show a positive normal force for a diverging wedge, which is the opposite sign predicted by the 1-D slider bearing.

To achieve both goals, we seek the simplest model that can capture the main physics of the problem and be solved quickly, because the problem will be iteratively solved in the design optimization processes. Since our experimental normal forces are due to viscous effects, this

suggests that the Reynolds equation [7] can be used for modeling our system instead of the full Navier-Stokes equations. The Reynolds equation is a single simplified form of the conservation of mass and momentum equations for incompressible Newtonian fluid flow. It neglects inertial effects and some spatial gradients of velocity and pressure due to a large difference of length scales in the problem (thin gap). Several numerical studies on the effects of surface textures have been performed using the Reynolds equation [8, 9, 10, 11, 12]. Journal bearings [13, 14], parallel sliders [15], and conforming contacting surfaces [16, 5] have been examined and show that the addition of surface textures can increase the load carrying capacity of these scenarios. Optimization studies have also been performed to determine an optimal texture profile [5, 17, 18, 19], although the optimal texture profile was selected from a specified set of allowable surface textures and not from a generic surface texture design space (e.g. arbitrarily parameterized surface height profiles, which we are pursuing [2]).

Optimization efforts require many numerical simulations to be performed. Therefore, we have considered the different numerical techniques available to solve the Reynolds equation and select a method that will achieve a sufficiently accurate solution for an acceptably low computational cost. The most commonly used methods for solving the Reynolds equation are the finite difference method (FDM) [8, 9, 10, 13, 14, 15, 16, 20, 21, 22], finite volume method (FVM) [22, 23], finite element method (FEM) [22, 24, 25], and spectral/pseudo-spectral method [22, 26, 27].

Each method has its own advantages and disadvantages (which are discussed in detail the Supplemental Information); for our work here, we use the pseudo-spectral method, which can give accurate solutions for a small number of grid points [22] due to the method's exponential error

convergence [28, 29, 30], allowing for faster simulations. Other methods could also have been used, as described above; however, we use the pseudo-spectral method because it guarantees that the pressure solution is continuous, differentiable, and integrable [31], which is important because we want to compare the normal force (integral of pressure) and shear stress (from derivatives of velocity, and thus derivatives of pressure) from simulations to experiments.

Design optimization is also aided by the smoothness of the pressure field (and stress field) calculated using the pseudo-spectral method. If the solution were non-smooth (for example, that calculated by the FDM), then the non-smooth mapping from design variables (surface texture profile) to objective function (friction) could result in numerical difficulties when attempting to use a gradient-based optimization algorithm. This problem can be resolved by using smooth approximation functions in the simulations, which the pseudo-spectral method does.

We describe implementation of the pseudo-spectral method to solve the steady-state Reynolds equation in cylindrical coordinates for generic surface textured thrust bearings. The numerical results are compared to an analytical solution and *non-trivial* experimental data [1, 3] to verify the numerical method. The experimental results show that the textured disks do not act like traditional slider bearings, meaning the work presented here is important for understanding the production of normal forces with textured disks. The agreement is not perfect, but the disagreement seems to come from experimental imperfection. Importantly, the model captures the sign and reasonable magnitude of the normal force (which previous models are unable to do). The verified numerical code is then used to determine the optimal asymmetric angle of a tilted elliptical "hole" texture for decreasing friction by finding the local minimum of the effective friction coefficient curve, which is a function of the gap, but not the sliding velocity in our model

formulation. This analysis is performed in the context of a thrust bearing, but is applicable to general applications with full-film lubrication.

2. Governing Equation

We model our system using the 2-D steady state Reynolds equation in cylindrical coordinates, which is derived from mass conservation for an incompressible fluid and the Navier-Stokes (conservation of momentum) equations in cylindrical coordinates [32], given as

$$\underline{\nabla} \bullet \underline{v} = 0 \tag{1}$$

$$\rho \frac{D\underline{v}}{Dt} = -\underline{\nabla} p + \eta \underline{\nabla}^2 \underline{v} \tag{2}$$

where ρ is the fluid density, p is the pressure, η is the fluid viscosity, $\underline{v}$ is the velocity vector, and $\frac{D}{Dt}$ is the material derivative. These equations can be simplified and combined through several assumptions that neglect certain gradients due to separation of length scales and a low Reynolds number (see Supplemental Information) to give

$$\frac{1}{r}\frac{\partial}{\partial r}\left(r h^3 \frac{\partial p}{\partial r} \right) + \frac{1}{r}\frac{\partial}{\partial \theta}\left(\frac{h^3}{r}\frac{\partial p}{\partial \theta} \right) = 6\eta\Omega \frac{\partial h}{\partial \theta}, \tag{3}$$

which is a linear, second order, non-constant coefficient partial differential equation for the pressure that satisfies both conservation of mass and momentum.

The velocity boundary conditions (coordinates in Figure 2) are

$$\begin{aligned} &\text{at } z=0\text{: } v_\theta = r\Omega \text{ and } v_r = v_z = 0 \\ &\text{at } z = h\text{: } v_\theta = v_r = v_z = 0 \end{aligned} \tag{4}$$

which from integrating conservation of momentum (see Supplemental Information) gives the velocity field as

$$v_r = \frac{1}{2\eta}\frac{\partial p}{\partial r}\left(z^2 - zh\right)$$
$$v_\theta = \frac{1}{2\eta}\frac{1}{r}\frac{\partial p}{\partial \theta}\left(z^2 - zh\right) + r\Omega\left(\frac{h-z}{h}\right). \quad (5)$$

If the gap height $h(r,\theta)$ is prescribed (and boundary conditions for the pressure in the r and θ directions are also prescribed) then Equation (3) can be solved explicitly for the pressure and used in Equation (5) to calculate the velocity field.

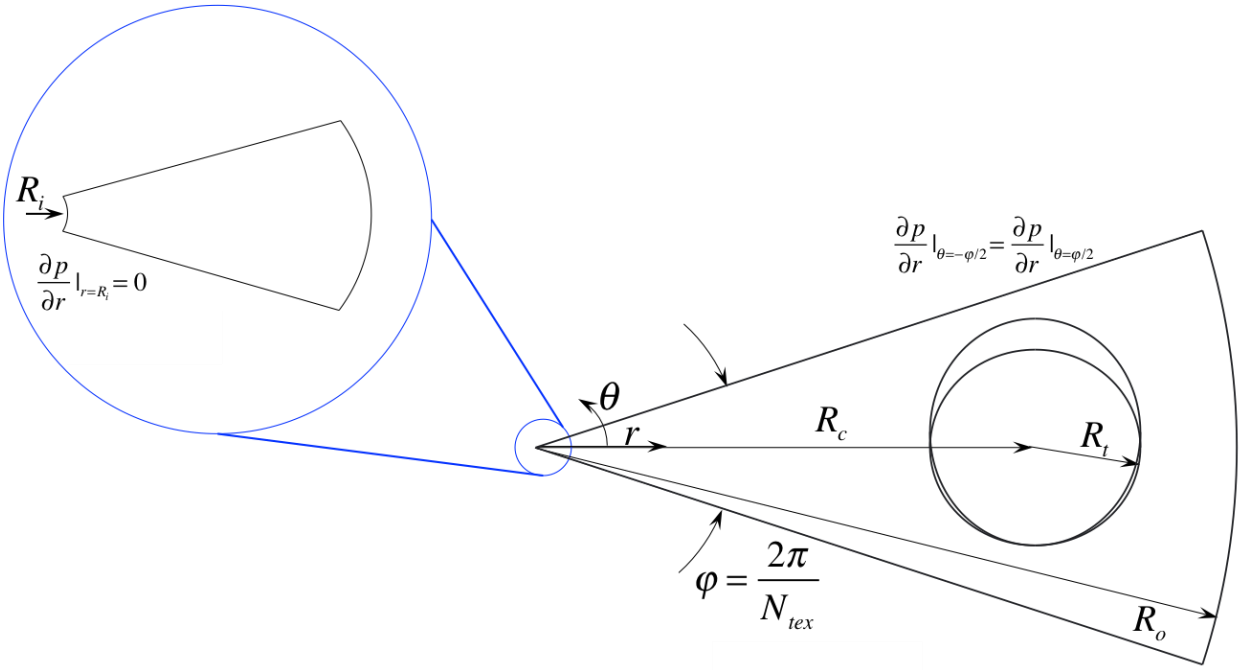

Figure 3: Diagram showing the geometric quantities used to define the simulated periodic surface textures. R_i is the inner radius, R_o is the outer radius, R_c is the radius to the center of the texture, R_t is the radius of the texture, and φ is the periodic spacing of the surface textures. Boundary conditions are also shown.

To solve Equation (3), boundary conditions on the pressure must be imposed, as shown in Figure 3. In the θ direction, we use periodic boundary conditions, given as

$$\begin{aligned} p\left(\theta = -\varphi/2\right) &= p\left(\theta = \varphi/2\right) \\ h^3\left(\theta = -\varphi/2\right)\frac{\partial p}{\partial \theta}|_{\theta=-\varphi/2} &= h^3\left(\theta = \varphi/2\right)\frac{\partial p}{\partial \theta}|_{\theta=\varphi/2}\,. \end{aligned} \tag{6}$$

where φ is the span in the θ direction of the periodic texture, and the h^3 front factor in front of the pressure gradient accounts for the possibility of a different gap height at the start and end of the periodic cell. At the inner radius, we impose a Neumann boundary condition, given as

$$\frac{\partial p}{\partial r}|_{r=R_i} = 0 \tag{7}$$

to impose symmetry and regularity in the physical space [33]. The boundary condition at the outer radius can either be Dirichlet $\left(p\left(r = R_0\right) = 0\right)$ or Neumann $\left(\frac{\partial p}{\partial r}|_{r=R_0} = 0\right)$; the selection of one over the other is non-trivial, and will be discussed in more detail in section 5.1.

3. Formulation and Solution Procedure

We write our own code for using the pseudo-spectral method to solve Equation (3) for the pressure so that it can be coupled to optimization tools (for optimization studies outside the scope of the work presented here [2]). The pseudo-spectral method solves the governing partial differential equation using a weighted residual technique (WRT) that computes an approximate solution to the differential equation [31, 34, 35]. The details of the solution method are given in the Supplemental Information. This includes the basis functions used in the approximation, numerical evaluations of the integrals used in the weak formulation, the resulting matrix form of the problem, and implementation of boundary conditions. The custom solver is written in

MATLAB™ and takes in a given gap height profile $h(r,\theta)$, fluid viscosity η, and angular velocity Ω and outputs the pressure profile $p(r,\theta)$.

The pressure obtained from the Reynolds equation solver will be used to calculate the normal force of the flat plate through an integration of the pressure over the area, calculated as

$$F_N = \int_0^{2\pi} \int_{R_i}^{R_o} p r dr d\theta, \tag{8}$$

and it can be seen that since inertial effects are negligible, normal force is proportional to viscosity and rotation speed

$$F_N \sim \eta\Omega. \tag{9}$$

Derivatives of pressure are used to determine the velocity field through Equation (5), and derivatives of velocity components determine the shear stress on the top plate

$$\tau_{\theta z}|_{z=0} = \eta\left(\frac{1}{r}\frac{\partial v_z}{\partial \theta} + \frac{\partial v_\theta}{\partial z}\right)|_{z=0}. \tag{10}$$

This is integrated to calculate the total shear load in terms of torque

$$M = \int_0^{2\pi} \int_{R_i}^{R_o} \left(r\tau_{\theta z}|_{z=0}\right) r dr d\theta, \tag{11}$$

and it can again be seen that the load scales linearly with viscosity and rotation speed

$$M \sim \eta\Omega. \tag{12}$$

Using the torque and the normal force, we define an effective friction coefficient μ^*, similar to previous work [1], as

$$\mu^* \equiv \frac{M / R}{F_N} \tag{13}$$

which is independent of the fluid viscosity or speed of rotation and only depends on the texture gap height profile.

To verify the solution method, the numerical solution is compared to an analytic solution of the Reynolds equation in the limit of a thin radial dimension. The analytic solution is obtained in the limit that $R_o - R_i << 1$, causing the pressure to not vary in the *r* direction, and that $h = h(\theta)$ only, which will be specified. We choose a linearly varying gap height profile and details of the profile are given in the Supplemental Information. These assumptions result in a 1-D ordinary differential equation for the pressure, allowing for an analytical solution to be obtained. Solving for the pressure and integrating in the *r* and θ directions gives the true normal force F_{true} as

$$F_{true} = \frac{3}{2}\eta\Omega {R_o}^2 \left(\frac{R_o\varphi}{h_1}\right)^2 \frac{\left(1-\left(\frac{R_i}{R_o}\right)^4\right)}{(1-\kappa)^2}\left(\ln(\kappa) + 2\left(\frac{1-\kappa}{1+\kappa}\right)\right) \tag{14}$$

where $\kappa = \frac{h_o}{h_1}$ and h_o and h_1 are the gap heights at the begging and end of the texture, respectively.

The numerical normal force on the flat plate is obtained using Gauss-Lobatto-Legendre quadrature on the computed pressure by $F_{comp} = \int_{-\varphi/2}^{\varphi/2}\int_{R_i}^{R_o} p_{comp} r dr d\theta$, where p_{comp} is calculated using the full 2-D form of the Reynolds equation (Equation (3)). The error between the computed normal force and the true normal force is calculated as

$$\varepsilon = \frac{|F_{true} - F_{comp}|}{|F_{true}|} \tag{15}$$

and is shown in Figure 4 for R_o=20 mm, R_o-R_i=10^{-6} mm, η=1.4 Pa s, and φ=π/5, Ω=10 rad/s, h_0=1 mm, and h_1=0.5 mm. The expected exponential decay in the error is observed [28, 29, 30],

verifying the numerical method. To validate the predictive capabilities, we compare to experiments with textured disks.

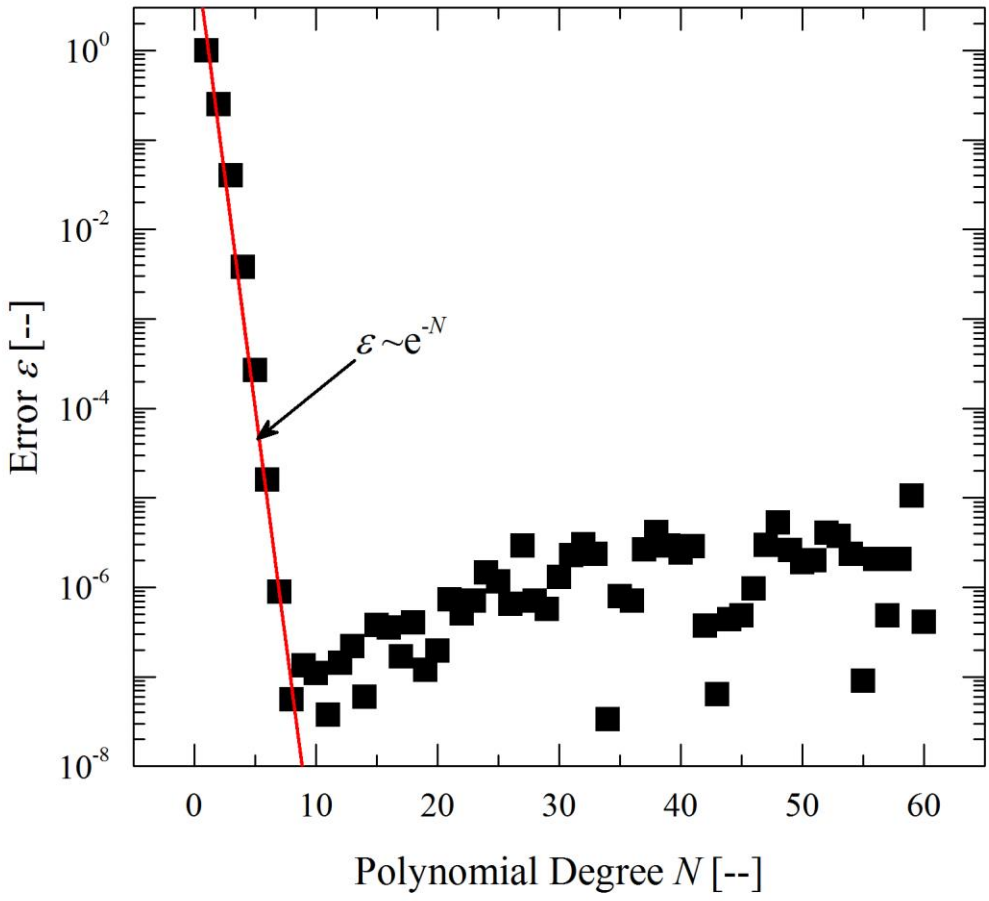

Figure 4: Error analysis of the computed solution compared to the analytic solution of the Reynolds equation for a thin strip (R_o-R_i=10^{-6}) defined in Equation (14). Conditions described in Section 3. Exponential decay is observed for the error, which matches the expected convergence rate for the numerical method used. We use N=65 for computations with the textured surfaces to avoid pixilation of the texture.

4. Textured Disk Modeling

In our previously measured experimental results for a surface textured thrust bearing [1], the surface textures are cylindrical holes cut at an angle β, which creates an elliptical top profile. We model our surface textures with an elliptical top profile, similar to the experiments. Figure 3 shows the geometric quantities used to define the surface textures; the finite inner radius is needed so that the $1/r$ terms do not diverge. We found that the normal force converged when R_i<0.02 mm (R_i/R_o<0.1%); details on this are given in the Supplemental Information. The geometric values for all the simulated textures are given in Table 1. Examples of the simulated texture surfaces are given in Figure 5.

Table 1: Geometric parameters used to define all the simulated surface textures.

Geometric Parameter	**Value**
R_i	0.01 mm
R_o	20 mm
R_c	14.25 mm
R_t	3 mm
φ	$2\pi/10$ rad

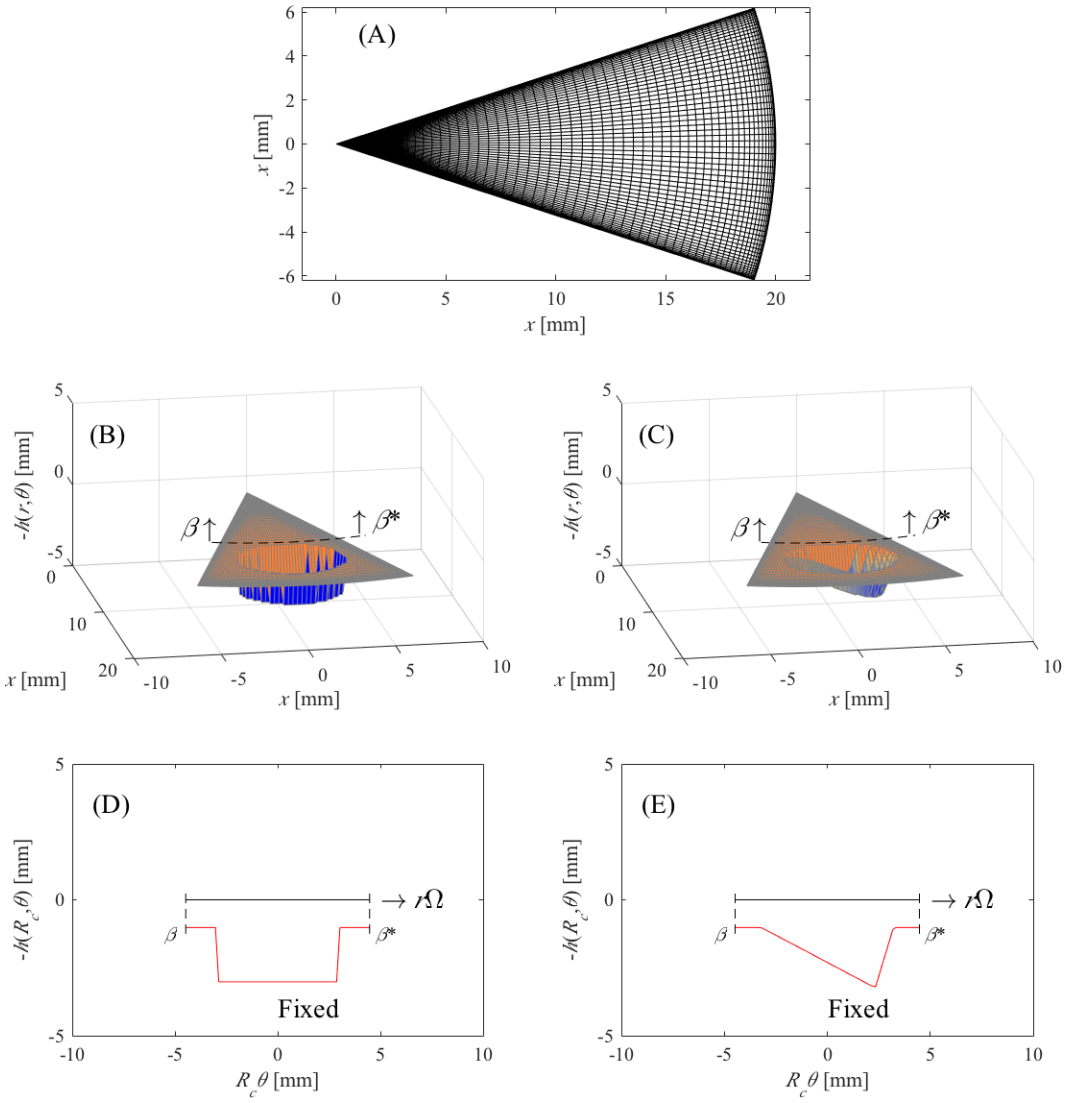

Figure 5: Simulated texture profiles. (A) spatial discretization used to simulate the textures. (B) symmetric texture. (C) asymmetric texture. (D)-(E) direction of motion for each surface texture. Asymmetric textures of varying angles were tested, including values given in Table 1 used in experiments by Schuh and Ewoldt [1].

4.1 Selecting Boundary Conditions

The boundary conditions in the θ direction used to solve the Reynolds equation are given in Equation (6). For the surface textures simulated, $h(\theta = -\varphi/2) = h(\theta = \varphi/2)$, which simplifies the θ boundary conditions to

$$\begin{aligned} p\left(\theta = -\varphi/2\right) &= p\left(\theta = \varphi/2\right) \\ \frac{\partial p}{\partial \theta}\Big|_{\theta=-\varphi/2} &= \frac{\partial p}{\partial \theta}\Big|_{\theta=\varphi/2} \end{aligned} \tag{16}$$

which is implemented numerically through B_ψ as

$$B_\psi = \begin{bmatrix} 0 & 0 & \dots & 0 & 1 \\ 1 & 0 & \dots & 0 & 0 \\ | & | & | & | & | \\ 0 & 0 & \dots & 1 & 0 \\ 0 & 0 & \dots & 0 & 1 \end{bmatrix}. \tag{17}$$

As previously stated, the boundary condition at the outer radius can be selected from either a Dirichlet (fixed pressure) or Neumann (fixed zero gradient in *r* direction) boundary condition. Previously, the Dirichlet boundary condition has been used [4, 40] where the pressure at the outer radius has been set to zero or atmospheric pressure (which may apply for textures surrounded by excess fluid). The Neumann boundary condition has not been used, but we argue here that it is the necessary boundary condition for our experiments and this choice may change the sign of the net normal force for some texture geometries. Since the Reynolds equation is a linear partial differential equation, the solution is heavily dependent on the boundary conditions used; therefore, we present a quick comparison between the two boundary conditions.

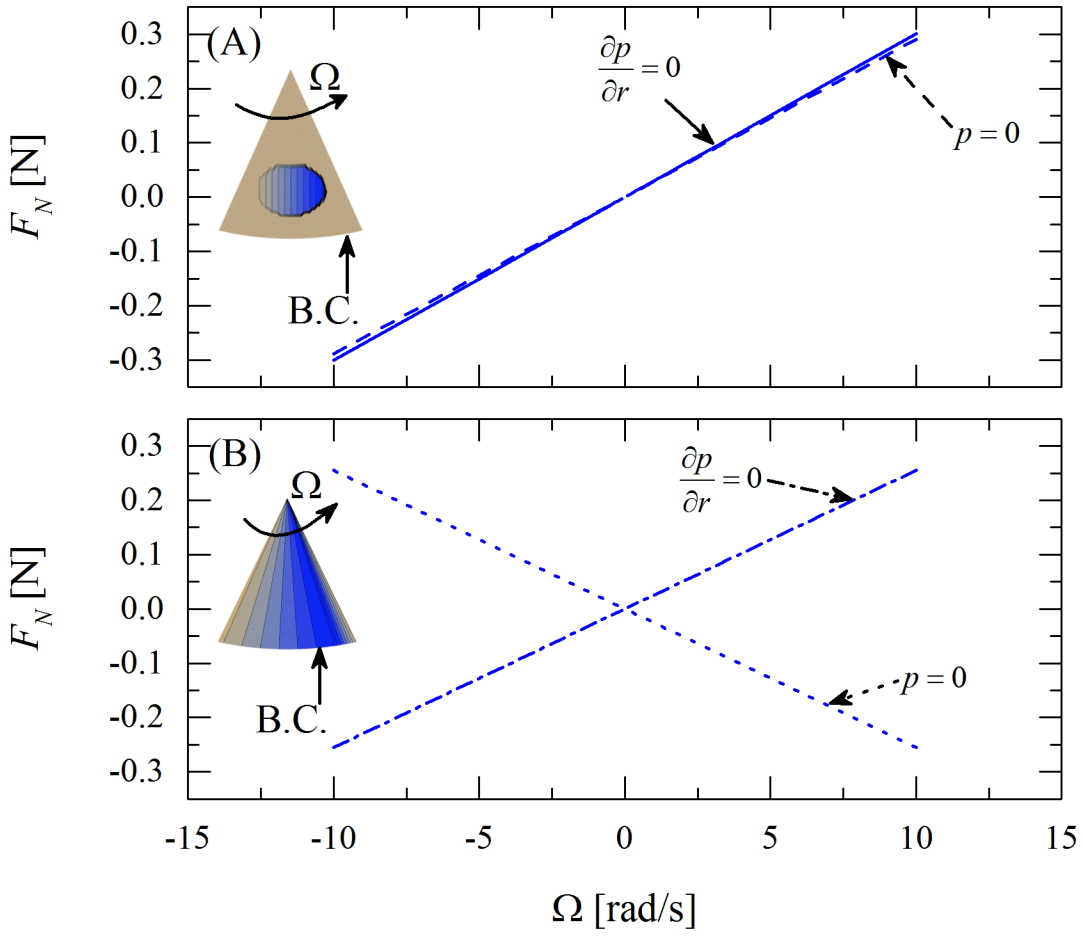

Figure 6: The sign of the normal force (thrust) is sensitive to boundary conditions, but only if the textured surface extends to the boundary. (A) a surface texture that extends over a finite area, and (B) a texture that extends to the boundary $r=R_o$ for h_0=269 μm and β=5.3°. When using the surface texture that extend over a finite area, changing boundary conditions does not change the sign of the normal force; however, changing the boundary conditions *changes* the sign of the normal force for a texture extending to the boundary $r=R_o$.

Figure 6 compares how the two boundary conditions affect the normal force when using the experimental surface textures and when using a textured profile that extends to the boundary $r=R_o$. When using the experimental surface textures, changing the boundary condition does not change the sign and magnitude of the normal force. This is because near the outer radius the texture

is flat, thus the flow is approximately boundary driven simple shear, causing only v_θ to be non-zero; this flow satisfies both boundary conditions, p=0 and $\frac{\partial p}{\partial r} = 0$ at r=R_o.

However, when using a surface texture that extends to the boundary r=R_o, the sign of the normal force changes when the boundary condition is changed. This is because using the Dirichlet boundary condition $p\left(r = R_o\right) = 0$ results in a zero pressure gradient in the flow direction $\frac{\partial p}{\partial \theta}|_{r=R_o} = 0$, thus from Equation (5) v_θ is only due to the drag flow and depends on the gap height h. If the gap height changes in the flow direction, $\frac{\partial h}{\partial \theta} \neq 0$, $\frac{\partial v_\theta}{\partial \theta} \neq 0$, and from mass conservation Equation (1) it may require $\frac{\partial v_r}{\partial r} \neq 0$. That is, there may be radial outflow or inflow for the p=0 Dirichlet boundary condition. In contrast, the Neumann boundary condition $\frac{\partial p}{\partial r}|_{r=R_o} = 0$, when used in Equation (5), removes the radial Poiseuille flow, $v_r = 0$ at r=R_o, corresponding to a zero radial flux boundary at the outer radius (Equation (5)).

We argue that, for the experiments of Schuh and Ewoldt [1], this zero-flux condition is most reasonable. In the experiments, there was an oil-air interface at the outer radius. The fluid inside the texture did not leave the textured domain and this impermeability is consistent with the Neumann boundary condition at the outer radius, which is implemented numerically through $B_r = I$. This causes the pressure to be known up to an arbitrary constant. We use the constraint that the average pressure along the outer edge is zero,

$$\frac{1}{\varphi}\int_{-\varphi/2}^{\varphi/2} p\left(R_o,\theta\right)d\theta = 0. \tag{18}$$

This can be interpreted as removing any surface tension pressure jump effects on the normal force, which was also done experimentally [1].

4.2 Resultant Normal and Shear Loads

We previously reported the experimental normal forces produced by the surface textures [1]. The simulated normal force is the integral of the total traction stress in the *z* direction,

$$F_N = N_{tex}\int_{-\varphi/2}^{\varphi/2}\int_{R_i}^{R_o}\left(p\,|_{z=0} - \tau_{zz}\,|_{z=0}\right)r dr d\theta \tag{19}$$

where N_{tex} is the total number of periodic cells on the thrust bearing, which sets the domain φ,

$$\varphi = \frac{2\pi}{N_{tex}} \tag{20}$$

and τ_{zz} is the shear stress on the *z* surface in the *z* direction, for a Newtonian fluid given as

$$\tau_{zz} = 2\eta\frac{\partial v_z}{\partial z}. \tag{21}$$

Using the continuity equation given in Equation (1) allows Equation (21) to be rewritten as

$$\tau_{zz} = 2\eta\left(-\frac{1}{r}\frac{\partial}{\partial r}\left(rv_r\right) - \frac{1}{r}\frac{\partial v_\theta}{\partial\theta}\right). \tag{22}$$

Substituting Equation (5) into Equation (22), performing the differentiation, and evaluating at *z*=0 gives

$$\tau_{zz}\,|_{z=0} = 0. \tag{23}$$

Substituting Equation (23) into Equation (19) and noting that the pressure is not a function of *z* (see assumptions in Supplemental Information) gives the final form of the computed normal force as

$$F_N = N_{tex} \int_{-\varphi/2}^{\varphi/2} \int_{R_i}^{R_o} pr dr d\theta. \tag{24}$$

For the shear load, we reported the apparent viscosity η_a measured with the surface textures which can also be mapped to the measured torque [1]. This involves an integration of the shear stress distribution, which itself depends on the velocity field. The velocity field is known after substituting the obtained pressure field into Equation (5). The shear stress $\tau_{\theta z}$ is the only contribution to the torque and is calculated for a Newtonian fluid as

$$\tau_{\theta z} = \eta \left(\frac{\partial v_\theta}{\partial z} + \frac{1}{r} \frac{\partial v_z}{\partial \theta} \right). \tag{25}$$

Scaling analysis can be performed on Equation (25) to determine the dominant effect in the shear stress calculation. Using the same non-dimensional values used to derive the Reynolds equation gives

$$\tau_{\theta z} = \frac{\eta \Omega R}{h_0} \left(\frac{\partial v_\theta^*}{\partial z^*} + \left(\frac{h_0}{R} \right)^2 \frac{1}{r^*} \frac{\partial v_z^*}{\partial \theta} \right). \tag{26}$$

The Reynolds equation was derived by neglecting all terms containing h_0 / R (and higher order powers of h_0 / R, see assumptions in Supplemental Information); therefore the term containing $(h_0 / R)^2$ in Equation (26) must also be neglected for the analysis to be consistent. This gives the shear stress as

$$\tau_{\theta z} = \eta \frac{\partial v_\theta}{\partial z}. \tag{27}$$

Substituting Equation (5) into Equation (27) allows the shear stress to be calculated as

$$\tau_{\theta z} = \frac{1}{2r}\frac{\partial p}{\partial \theta}\left(2z - h\right) - \frac{\eta \Omega r}{h} \tag{28}$$

The apparent viscosity that we previously reported [1] was obtained through the measurement of the shear stress on the flat plate, which is obtained numerically by evaluating Equation (28) at z=0, giving

$$\tau_{\theta z}\,|_{z=0} = -\frac{1}{2r}\frac{\partial p}{\partial \theta}h - \frac{\eta \Omega r}{h} \tag{29}$$

where the negative sign on the drag flow term indicates that this portion of the shear stress acts in the opposite direction of the motion **Ω**.

The resultant torque M on the flat plate is calculated from a torque balance on the flat plate

$$M = \int_0^{2\pi}\int_0^{R} \tau_{\theta z}\,|_{z=0}\; r^2 dr d\theta. \tag{30}$$

For comparisons with N_{tex} periodic domains this is

$$M_{comp} = N_{tex}\int_{-\varphi/2}^{\varphi/2}\int_{R_i}^{R_o} \tau_{\theta z}\,|_{z=0}\; r^2 dr d\theta. \tag{31}$$

For comparisons to our experimental results, the torque M is used to calculate the apparent viscosity as if the disks were separated by the nominal (minimal) gap h_0 [41] as

$$\eta_a = \frac{2h_0}{\pi R^4}\frac{M}{\Omega}. \tag{32}$$

4.3 Limitations of the Reynolds Equation

We can only compare the simulations to the experiments where the Reynolds equation is valid. Figure 7 shows the bounds where the Reynolds equation applies. Figure 7A shows the lines where

$$\mathrm{Re}_h \equiv \frac{\rho \Omega R_o h}{\eta} < 0.1 \tag{33}$$

$$Na \equiv \frac{(\Omega R_o)^2}{\kappa} \frac{\partial \eta}{\partial T} \approx \frac{\Delta \eta}{\eta} < 0.1 \tag{34}$$

$$\frac{h}{R_o} < 0.1 \tag{35}$$

where ρ is the density of the fluid, η is the viscosity of the fluid, and κ is the thermal conductivity of the fluid. Of particular note is Equation (34) to neglect viscous heating effects that cause viscosity change, which was observed under some experimental conditions [1] (Assumption 4, Supplemental Information).

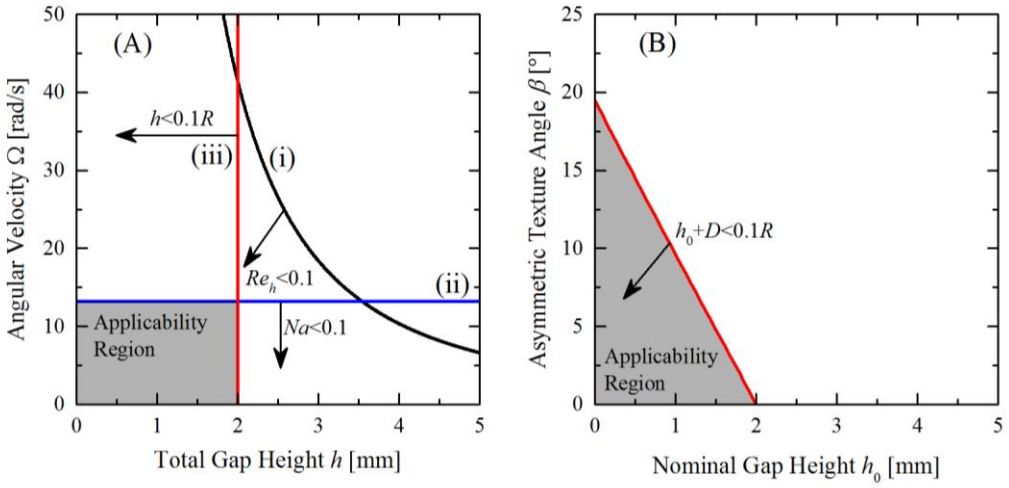

Figure 7: Approximate regions of applicability (shaded are) for the Reynolds equation using three key criteria: (i) Re<0.1 (Equation (33)) to neglect inertia, (ii) Na<0.1 (Equation (34)) to neglect viscous heating, (iii) $h<0.1R$ (Equation (35)) to neglect velocity gradients in the flow direction. (A) angular velocity Ω versus total gap height $h=h_0+D$. (B) angle of asymmetry β versus nominal gap height h_0 for $h<0.1R$.

Figure 7 shows these limits visualized as a window of operational conditions for validity of the Reynolds equation (shaded regions). Figure 7A shows all three criteria. Notably, the low Reynolds number criterion is not the limiting condition. The small gap requirement depends on the asymmetry angle β, as is shown in Figure 7B, which gives the maximum asymmetric angle β for a given nominal gap height such that Equation (35) is satisfied. For all the validity conditions, the thresholds could be set to smaller values for even more accurate modeling expectations.

5. Results for Textured Disks

The results from the Reynolds equation solver can be used to give general predictions for the performance of a surface texture in lubricated sliding. Figure 8 gives example fields that can be calculated after solving the Reynolds equation (fields calculated with other surface textures are given in the Supplemental Information). Both the velocity field and the pressure field are obtained, which can be used to give the shear stress on the moving plate. Both will be used in calculating the torque and normal force (example calculations are given in the Supplemental Information), which will be used to give the general performance of the surface texture. The simulated results can also be compared to experimental values by using the same input parameters used in the experiments.

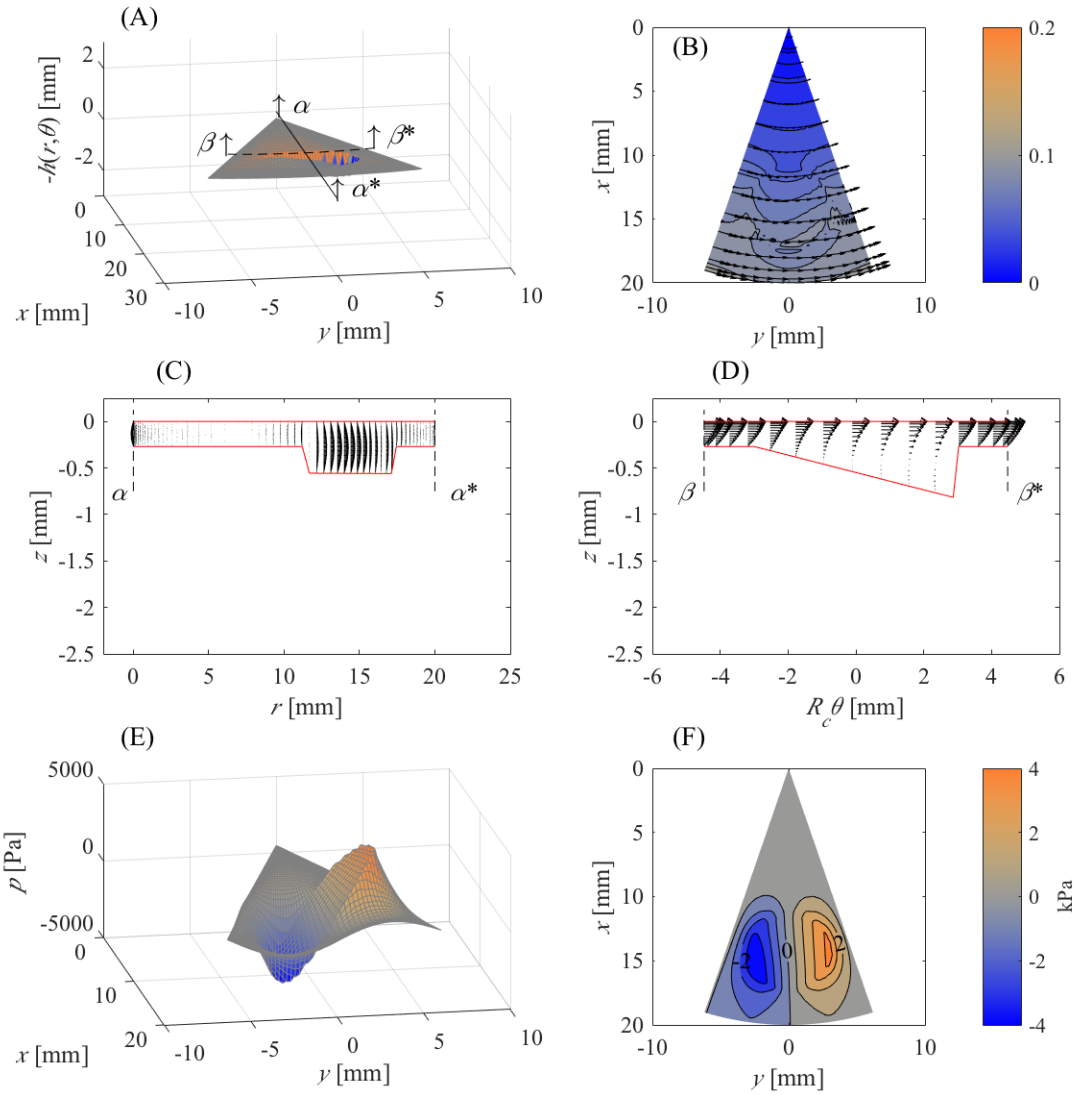

Figure 8: Example computed fields obtained with the Reynolds equation (see Supplemental Information Figures S3-S7 for additional examples). The example here is for an asymmetric surface texture with β=5.3° and Ω=10 rad/s at h_0=269 μm, which fall within the regions of applicability given in Figure 7. α-α^* is the line for θ=0. β-β^* is the line for r=R_t. These computed velocity and pressure fields were obtained for each texture tested with input values given in Table 2. (A) surface texture profile, plotted as -h. (B) plot of the velocity field at z=h_0/2. (C) velocity

field of v_r and v_z at θ=0°. (D) velocity field of v_θ and v_z at $r=R_t$. (E) computed pressure profile. (F) contour of pressure.

5.1 General surface texture performance

The simulations were run with bi-direction sliding, just as in the experiments [1]; Figure 9 shows the non-dimensional output parameters obtained with the Reynolds equation solver with R_t=3 mm, R_o=20 mm, and R_c=14.25 mm; β was fixed, and h_0 was varied. Figure 9A gives the non-dimensional shear stress, defined as

$$\tau^* = \frac{\eta_a}{\eta}. \tag{36}$$

As β increases, the non-dimensional shear stress decreases. This can be understood by the simple explanation that a larger angle increases the texture depth, and this decreases the *local* shear rate inside the surface texture. This reduction in local shear rate leads to a reduction in local shear stress. This texture effect is more pronounced for smaller nominal gap height h_0, thus the non-dimensional shear stress also decreases as h_0 decreases. At large values of h_0, the effect of the texture is smaller, because the local gap height is not changing very much. At smaller values of h_0, the effect of the textures become more pronounced, leading to a reduction in the shear stress.

Figure 9B gives the non-dimensional normal force, defined as

$$F_N{}^* = \frac{F_N}{\pi R_o{}^2 \left(\frac{\eta R_o \Omega}{h_0} \right) \left(\frac{R_o}{h_0} \right)}. \tag{37}$$

If we define $\kappa \equiv D / h_0 + 1$, where κ is used in Section 3 to obtain the expression for the analytical normal force, we can rewrite the expected scaling for the normal force in Equation (14) as

$$F_N \sim \frac{1}{\left(D/h_0\right)^2}\left(\ln\left(D/h_0+1\right)-2\frac{D/h_0}{D/h_0+2}\right). \tag{38}$$

The non-dimensional normal force in Figure 9B follows this scaling. When h_0 is very large, the effect of the texture is very small, causing the normal force to go to 0. As h_0 decreases, the normal force increases until it goes through a local maximum (suggesting an optimal D/h_0) and then decays to 0, as predicted by Equation (38).

Figure 9C gives the coefficient of friction, defined using Equation (13), which is essentially the ratio between the non-dimensional shear stress and the non-dimensional normal force. The coefficient of friction increases with β due to the reduction in normal force seen in Figure 9B, but then plateaus due to the reduction in both the shear stress and the normal force. The simulations are able to correctly predict the sign of the normal force (Figure 2 and Figure 9B), which the simple 1-D Cartesian models were unable to do.

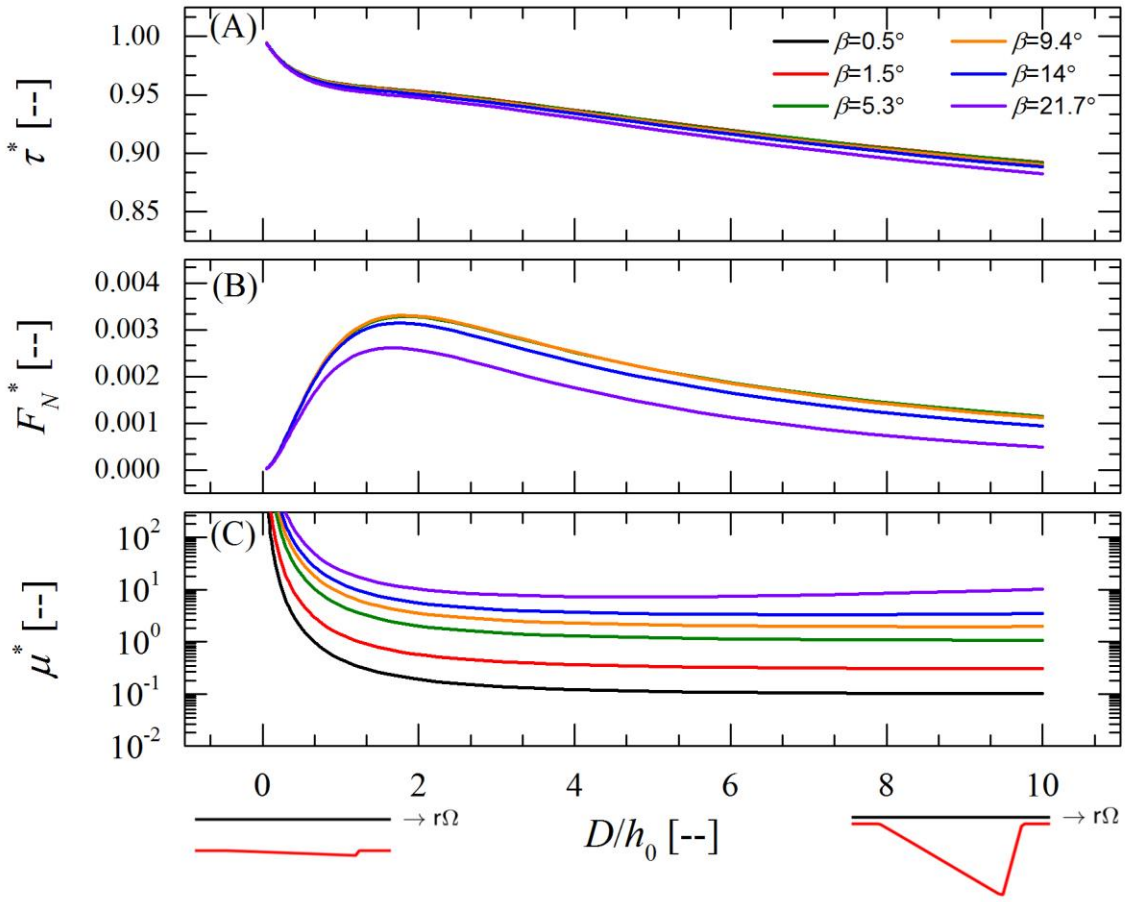

Figure 9: Prediction for varying dimensionless gap height D/h_0 for fixed angle β where $D = 2R_t \sin(\beta)$ from the Reynolds equation solver where R_t=3 mm, R_o=20 mm, and R_c=14.25 mm. (A) non-dimensional shear stress (Equation (36)). (B) non-dimensional normal force (Equation (37)). (C) coefficient of friction (Equation (13)). The simulations are able to predict the correct sign of the normal force (compare with Figure 2), which simple 1-D Cartesian models are unable to do.

In the experiments, h_0 was fixed, and β was varied. Figure 10 shows the non-dimensional parameters obtained from the Reynolds equation solver, again for R_t=3 mm, R_o=20 mm, and R_c=14.25 mm, but for fixed h_0 and varied β. Figure 10A gives the non-dimensional shear stress. At larger nominal gap heights, the textures do not reduce the local shear stress as much as at smaller gap heights, resulting in a larger shear stress reduction at smaller nominal gap heights. Figure 10B gives the non-dimensional normal force, and shows that for each gap height, there is an optimal β for producing a normal force with asymmetric surface textures. This change in the optimal β can be explained through Figure 9B, where the optimal D/h_0 is independent of β. Therefore, as h_0 changes, the optimal β must also change for the optimal D/h_0 to remain constant. The scatter in the data is most likely due to competing effects of increasing β on increasing D/h_0 (Figure 9), resulting in a smaller normal force, while also increasing the size of the surface texture, resulting in a larger normal force. Figure 10C gives the coefficient of friction, and also shows that for each gap height, there is an optimal β for decreasing friction with asymmetric surface textures. The scatter in the friction coefficient comes from the scatter in the normal force.

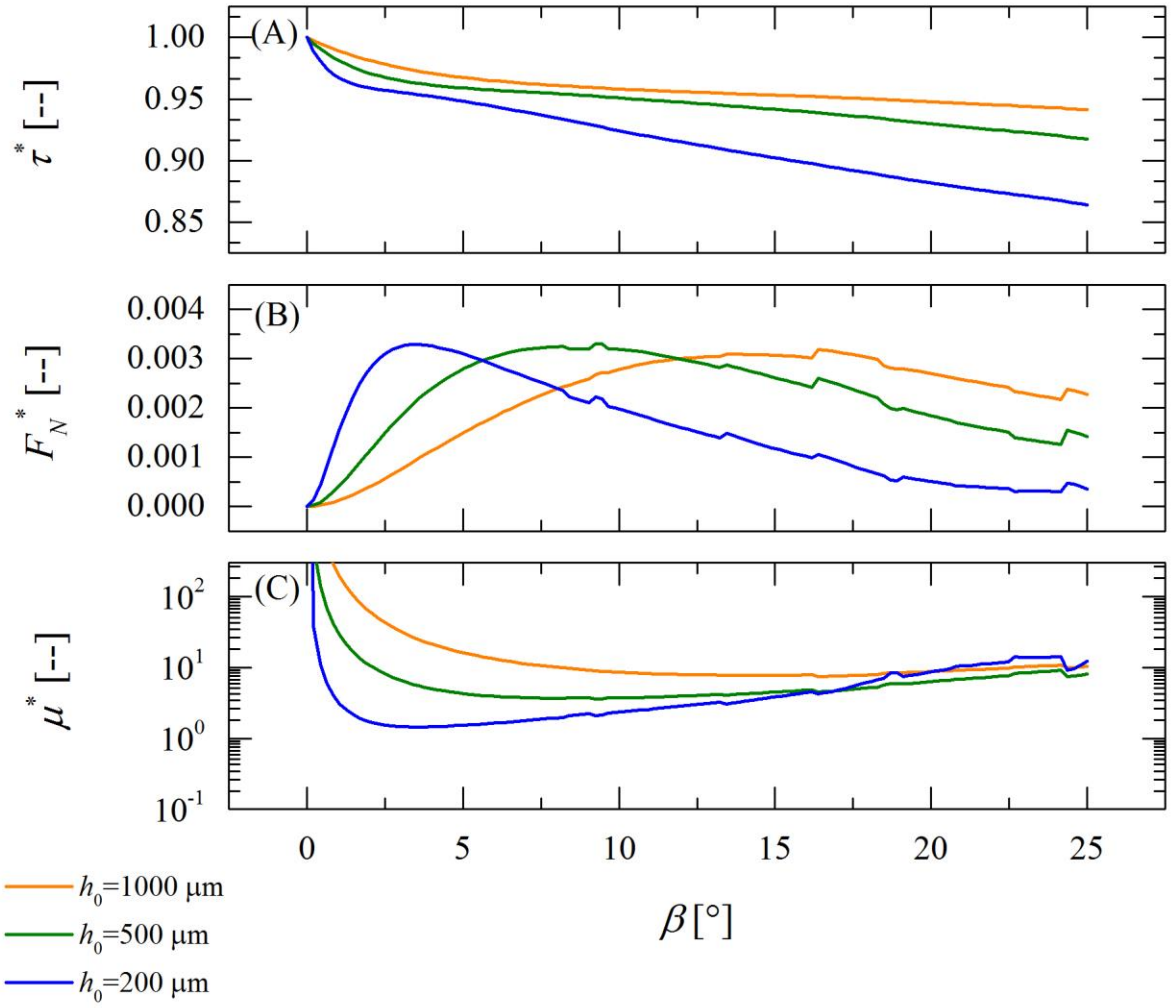

Figure 10: Predictions for varying angle β with fixed texture cylindrical radius R_t and varying h_0; R_t=3 mm, R_o=20 mm, and R_c=14.25 mm. (A) non-dimensional shear stress (Equation (36)). (B) non-dimensional normal force (Equation (37)). (C) coefficient of friction (Equation (13)). At each gap height, an optimal value of β is found for producing a normal force and decreasing the coefficient of friction.

Table 2: Input parameters for simulations when comparing to experiments of Schuh and Ewoldt [1].

Parameter	Input Values
h_0	1019, 519, 269 μm
$\|\Omega\|$	[0.1,10] rad/s
β	5.3°, 9.4°, 14°, 21.7°

5.2 Comparison to experiments

We want to compare theoretical predictions for surface texture performance to experimental results [1]. The same input parameters used in the experiments are also used in the simulations, and the input values used are given in Table 2. Supplemental Information (Figures S11-S13) give general predictions for these experimental conditions, and we make direct comparison to experiments here in Figures 11, 12, and 14.

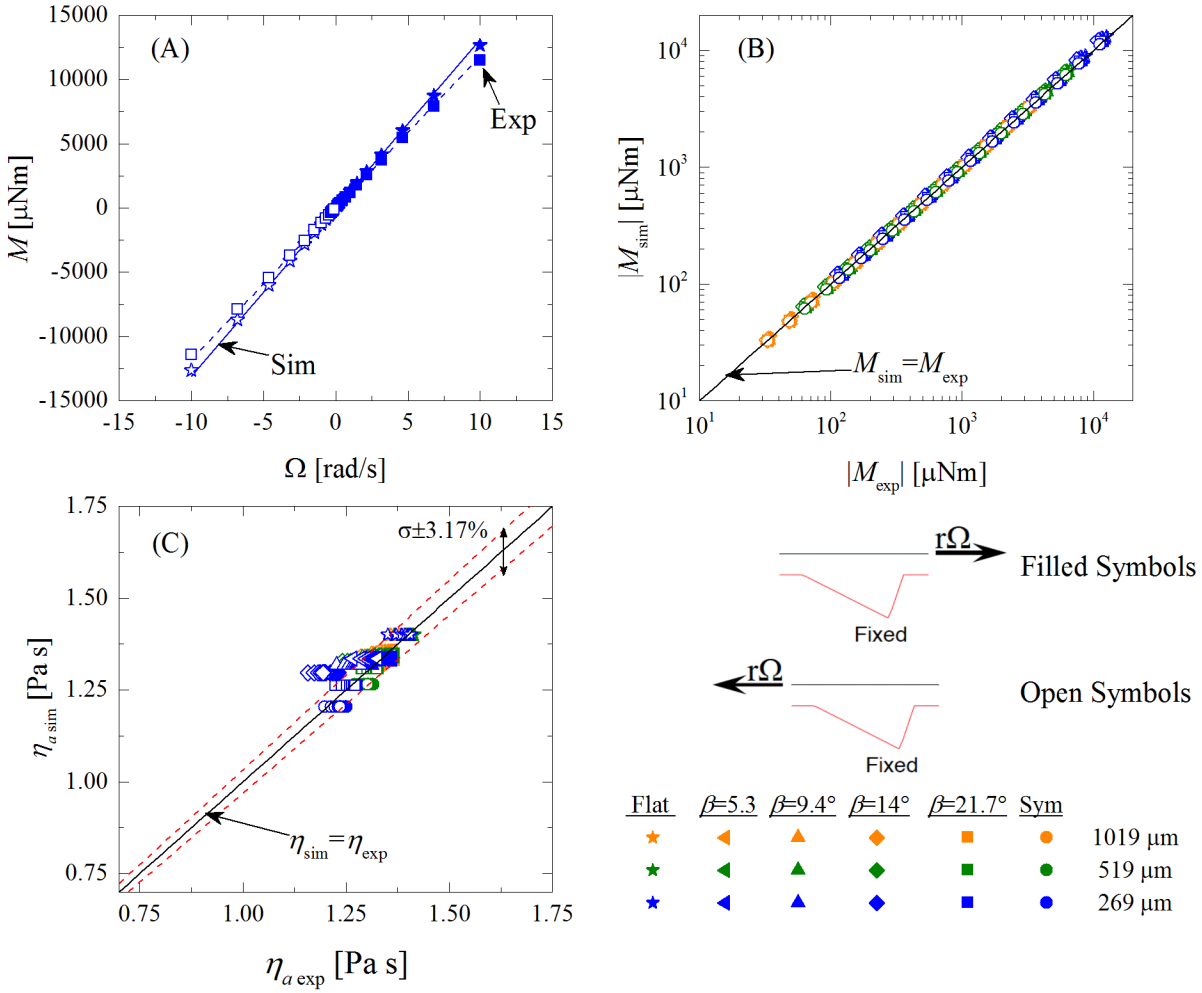

Figure 11: Comparison of the shear forces obtained from simulation, "sim", to experimentally measured shear , "exp" (from Schuh and Ewoldt [1]). (A) Comparison of sign and magnitude of torque M for flat plate and β=21.7° at h_0=269 μm. (B) Comparison of magnitude of torque for all textures at all gap heights tested, including textures outside the applicability region of the Reynolds equation. (C) Comparison of apparent viscosity for all textures tested at all gap heights, including textures outside the applicability region of the Reynolds equation. The standard deviation (Equation (40)**)** is σ=3.17% around the systematic error of ε_{sys}=-0.117% when using all experimental data points.

5.2.1 Torque Comparison

Figure 11 shows the comparison between the experimentally measured torque (and apparent viscosity) with the highly refined mineral oil S600 [1, 3] and the apparent viscosity obtained from simulations. (Results from the simulations for torque as a function of different β and Ω are given in Figure S11 in the Supplemental Information). No fit parameters are used. Also shown is a line where the apparent viscosity obtained with the Reynolds equation equals the experimental apparent viscosity. Figure 11A compares the sign and magnitude of the torque for the flat plate and β=21.7°. Figure 11B compares the magnitude of the torque for all surface textured tested, and includes data outside the applicability region of the Reynolds equation. Systematic error, calculated as

$$\varepsilon_{sys} = \frac{1}{N}\sum_{i=1}^{N}\frac{\eta_{\mathrm{exp},i} - \eta_{\mathrm{sim},i}}{\eta_{\mathrm{sim},i}} \tag{39}$$

is $\varepsilon_{sys} = -0.117\%$ when using data from all the surface textures tested. The standard deviation σ between the simulations and the experiments around the systematic error is given as a percentage and is calculated as

$$\sigma = \sqrt{\frac{1}{N}\sum_{i=1}^{N}\frac{\left(\eta_{\mathrm{sim},i} - \dfrac{\eta_{\mathrm{exp},i}}{1+\varepsilon_{sys}}\right)^2}{\eta_{\mathrm{sim},i}^{\,2}}}\,. \tag{40}$$

When using all the surface textures, $\sigma = 3.17\%$. Figure 11C compares the apparent viscosity between the experiments and the simulations for all the textures tested.

Systematic error can also be calculated only using those textures where the Reynolds equation applies, giving $\varepsilon_{sys} = -1.15\%$, and the standard deviation around the systematic error is $\sigma = 2.35\%$.

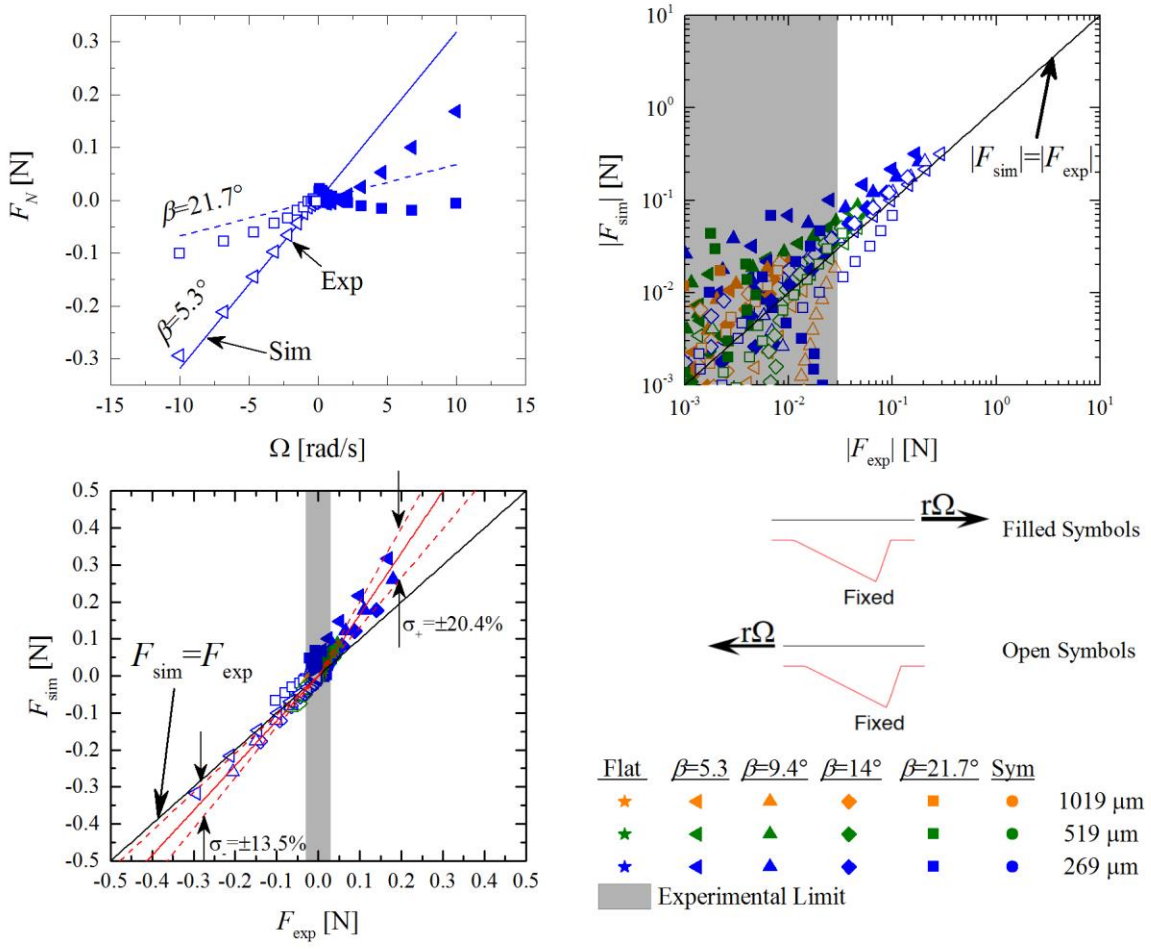

Figure 12: Comparison of the normal forces from simulation, "sim" to those measured experimentally measured, "exp" (Schuh and Ewoldt [1]). (A) Magnitude and sign comparison for β=5.3° and β=21.7° at h_0=269 μm. (B) Magnitude comparison for all textures tested. (C) Magnitude and sign comparison for all textures, including those outside the range of applicability.

The standard deviation (Equation (42)) σ_+=20.4% around the systematic error of ε_{sys}=-39.9% when sliding in the direction of the filled symbols and σ_-=13.5% around the systematic error of ε_{sys}=-17.5% when sliding in the direction of the open symbols when using all the textures and when using only those within the region of applicability.

5.2.2 Normal Force Comparison

Figure 12 shows the comparison between the experimentally measured normal force and the simulated normal force. (Results from the simulations for normal force as a function of different β and Ω are given in Figure S12 in the supplemental information). Also shown is the line where the simulated normal force would equal the experimentally measured normal force. Figure 12A compares the magnitude and the sign of the normal force for β=5.3° and β=21.7° at h_0=269 μm. The simulations produce the correct sign that is observed in the experiments, in contrast to the simple 1-D Cartesian models (Figure 2).

Systematic error, calculated as

$$\varepsilon_{sys} = \frac{1}{N}\sum_{i=1}^{N}\frac{F_{\text{exp},i} - F_{\text{sim},i}}{F_{\text{sim},i}} \tag{41}$$

is $\varepsilon_{sys,+} = -39.9\%$ when sliding in the direction of the filled symbols (positive normal force) and $\varepsilon_{sys,-} = -17.5\%$ when sliding in the direction of the open symbols (negative normal force), both of which are higher than the systematic error in the torque.

The systematic error in the normal force is most likely due to the neglecting of τ_{zz} and changes in p as a function of z that were neglected in deriving the Reynolds equation, as well as neglecting changes in viscosity that could also lower the magnitude of the pressure, and thus lower

the magnitude of the normal force. There could also be a systematic error in the experiments; the simulations predict odd symmetry when the direction of motion is flipped, which is not seen in the experiments. This could be due to an error in the inertial correction for the experiments; the same inertial correction for parallel flat plates was used for the surface textures, which could introduce a systematic error in the experiments that depends on direction of rotation.

The standard deviation σ between the experiments and the simulations around the systematic error is again given as a percentage and is calculated as

$$\sigma = \sqrt{\frac{1}{N}\sum_{i=1}^{N}\frac{\left(F_{\text{sim},i} - \dfrac{F_{\text{exp},i}}{(1+\varepsilon_{sys})}\right)^2}{F_{\text{sim},i}^{\,2}}} \tag{42}$$

and only the normal force values that are above the experimental measurement limit are used. The deviation about the systematic error is found to be $\sigma_+ = \pm 20.4\%$ for positive normal force and $\sigma_- = \pm 13.5\%$ for negative normal force. Figure 12B shows the comparison of just the magnitude of the normal force. Figure 12C shows the comparison of the magnitude and sign of the normal forces for all the textures tested, including those where the Reynolds equation is not valid.

The systematic error and the standard deviation can also be calculated using only those textures where the Reynolds equation applies. Again, the standard deviation about the systematic error is found to be $\sigma_+ = \pm 20.4\%$ for positive normal force and $\sigma_- = \pm 13.5\%$ for negative normal force. These results are the same because the normal force values for the textures outside the applicability range of the Reynolds equation are all below the experimental resolution limit.

5.2.3 Rationale for Sign of Normal Force

We wish to understand the difference between the sign of the normal force from the 1-D theories and 2-D simulations. We start by examining the pressure gradient in 1-D, which can be understood by using conservation of mass coupled with the concept that the velocity field is a linear combination of boundary-driven (Couette) and pressure-driven (Poiseuille) flow. In 1-D, the volumetric flow rate everywhere inside the texture must be a constant

$$Q = Q_{drag} + Q_{pressure} = \text{Constant} \tag{43}$$

where the drag flow term appears as average velocity times the gap height,

$$Q_{drag} = \frac{U}{2} h(x) \tag{44}$$

and the pressure driven flow term depends cubically on the local gap height

$$Q_{drag} = -\frac{1}{12\eta} \frac{dp}{dx} h^3(x). \tag{45}$$

For a changing gap height $h(x)$, the drag flow term Q_{drag} will change. For example, an increasing gap in the direction of the flow, i.e. $\frac{dh}{dx} > 0$, *increases* Q_{drag}. To keep the total flow rate constant, $Q_{pressure}$ must also change. For example, an increasing gap height $\frac{dh}{dx} > 0$ that causes an increase in Q_{drag} requires a decrease in $Q_{pressure}$. This decrease in $Q_{pressure}$ could be either a smaller positive flow rate or a more negative flow rate, depending on the sign of $\frac{dp}{dx}$. The resulting local pressure gradient $\frac{dp}{dx}$ changes to perfectly accommodate Q=Constant. The change in the pressure gradient as the gap height changes can be found by differentiating Equation (43).

Differentiating Equation (43), and writing in terms of the pressure gradient, we have

$$\frac{d}{dx}\left(\frac{dp}{dx}\right)=\left(\frac{6\eta U}{h^3}-\frac{3}{h}\frac{dp}{dx}\right)\frac{dh}{dx}. \tag{46}$$

When h is known, Equation (46) is a 1st order linear, non-constant coefficient, non-homogeneous ordinary differential equation for the pressure gradient $\frac{dp}{dx}$.

The concavity of the pressure can be determined by examining Equation (46). In the Reynolds equation, we assume that $h<<1$, meaning the $1/h^3$ term typically dominates the $1/h$ term. In such a case, the sign of the concavity of the pressure field is determined by the sign of $\frac{dh}{dx}$. When $\frac{dh}{dx}>0$ (slow expansion) the pressure has positive concavity, and when $\frac{dh}{dx}<0$ (slow contraction) the pressure has negative concavity.

Enforcing the boundary conditions, in 1-D at $x=0$ and $x=L$, will set the sign of the pressure. In the slow expansion motion (see Figure 2B) the pressure has positive concavity and with $p(x=0)=p(x=L)=0$ [42, 43], the pressure must be negative everywhere, resulting in a net negative normal force. This is akin to a typical thrust bearing operating in the wrong direction. We observe in experiment and (2-D) simulation that this same direction of motion (slow expansion) causes a *positive* net normal force with our textured surface. What changes in 2-D?

In 2-D, the general rationale for the concavity of the pressure field is similar to 1-D, although conservation of mass is less strict in the θ direction, because there can also be flow in the r direction. More importantly, the pressure is also not restricted to be zero at $\theta=-\varphi/2$ and $\theta=\varphi/2$.

As seen in Figure 13, the general trend of the pressure profile is the same between the 1-D and 2-D cases, where the pressure has a positive concavity in the direction of slow expansion and a negative concavity in the direction of slow contraction. The concavity alone cannot predict a net

positive or negative pressure; the boundary conditions will determine the upward/downward shift of the concave pressure profile. Figure 13 shows the average pressure for the different sliding directions and boundary conditions at the outer edge where

$$p^* = \frac{p}{\frac{\eta |U|}{h_0}} \tag{47}$$

for the 1-D case and

$$p^* = \frac{p}{\frac{\eta R_o |\Omega|}{h_0}} \tag{48}$$

for the 2-D case.

The average pressure is much closer to zero in the 2-D case. This can be understood by considering that the edge boundary condition on pressure is either zero everywhere, or its average is zero. When the boundary condition at the outer edge is changed, the sign of the average pressure also changes, and the sign of the average pressure correlates to the sign of the normal force.

In the 1-D case, the sign of the normal force is set by where the pressure is equal to zero. This matches results given by Dobrica and Fillon [23] who showed that in 1-D the sign of the normal force can be changed by changing the location of zero pressure. In 2-D, the sign of the normal force is set by the boundary condition at the outer edge, which has no analog in 1-D. The average pressure is closer to zero, and the direction of shift to net positive or net negative, due to the different boundary conditions, is difficult to predict. Therefore, we should expect the pressure gradient between 1-D and 2-D to have similar trends, but the sign of the normal force may not be the same, due to changing the location of where the pressure equals zero.

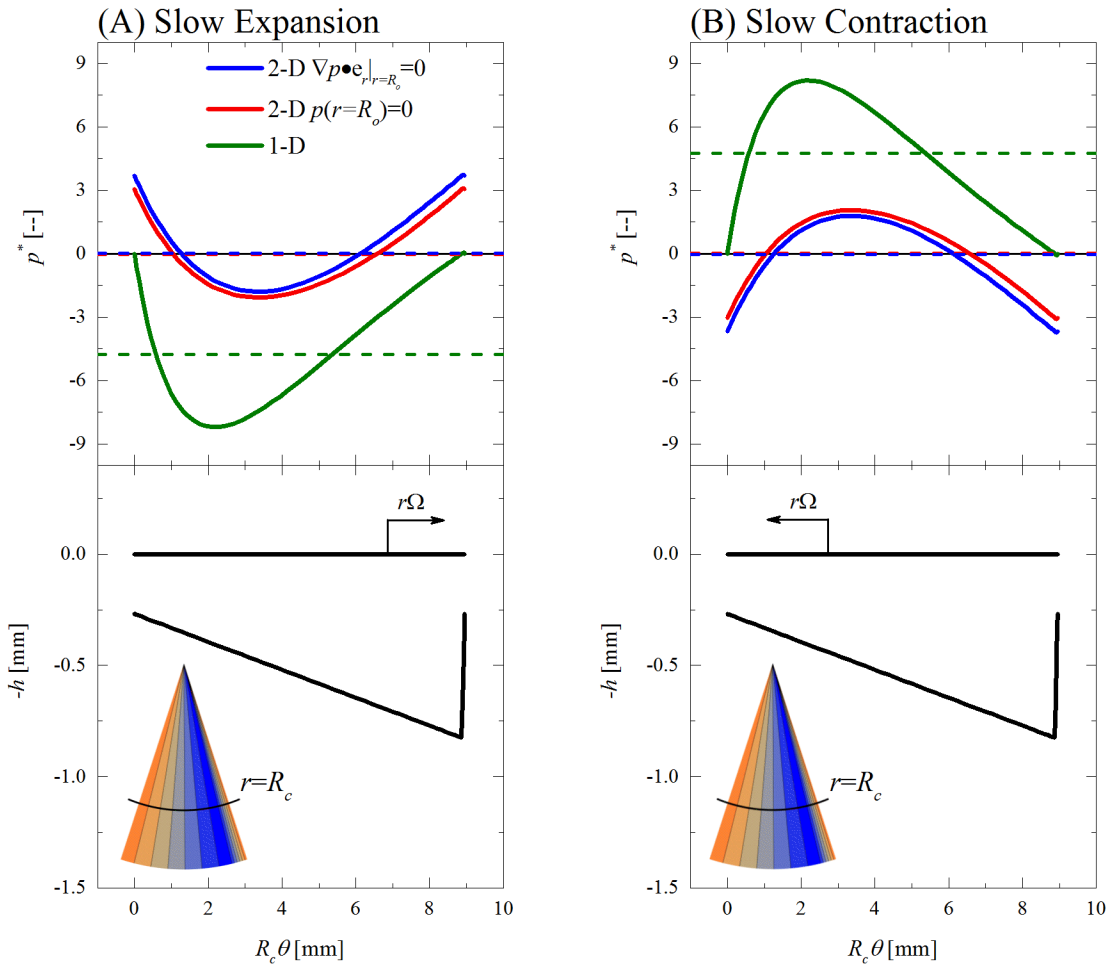

Figure 13: Pressure concavity and sign of net normal force in two different directions of motion: (A) slow expansion, (B) slow contraction. Comparison between standard 1-D slider bearing theory (green) and a 2-D periodic pie slice wedge (red and blue) (same geometry as used in Figure 6B). Pressure profile for 2-D case is from a specific radius (r=14.25 mm). The pressure concavity (sign of second derivative) is the same for all cases (dependent on direction of motion only), but the average pressure (dashed lines) depend on the geometry and boundary conditions. The 2-D wedge with Neumann pressure condition at the outer boundary has opposite sign to the standard slider bearing theory, consistent with Figure 6B.

6 Optimal β for Asymmetric Textures

The previous sections have verified our modeling and numerical simulation and also rationalized the sign of the experimentally observed normal forces. The experiments of Schuh and Ewoldt [1] suggested an optimal asymmetry angle β. We can now use our computations to determine the optimal β angle for decreasing friction with these asymmetric surface textures. The optimal condition minimizes the effective friction coefficient (Equation (13)). In this analysis, only β varies at different gap heights h_0; all other geometric and flow variables were held constant.

Figure 14 shows μ^* as a function of β for both the experiments and the simulations at all the gap heights tested with rotational speed $\boldsymbol{\Omega}$=10 rad/s (this speed is chosen to be high enough for the normal force to be above the experimental force measurement limits, but low enough to avoid viscous heating). (Results from the simulations for μ^* as a function of different β and Ω are given in Figure S13 in the supplemental information.) Error bars are shown for the experimental values using propagation of error in the normal force and torque measurement as

$$\sigma_{\mu^*}{}^2 = \left(\frac{\partial \mu^*}{\partial M}\right)^2 \sigma_M{}^2 + \left(\frac{\partial \mu^*}{\partial F_N}\right)^2 \sigma_{F_N}{}^2. \tag{49}$$

Substituting Equation (13) into Equation (49) and simplifying gives

$$\sigma_{\mu^*} = \mu^* \sqrt{\left(\frac{\sigma_M}{M}\right)^2 + \left(\frac{\sigma_{F_N}}{F_N}\right)^2}. \tag{50}$$

Agreement is seen between the experiments and the simulations in the region where the Reynolds equation is valid. However, the computed values are always below the experimental values; this is because the simulations have a larger normal force with larger deviation than the torque, and the normal force is in the denominator. The optimal β is dependent on the nominal gap height,

suggesting that there is an optimal h_0 / D ratio, similar to that predicted by slider bearing theory [7].

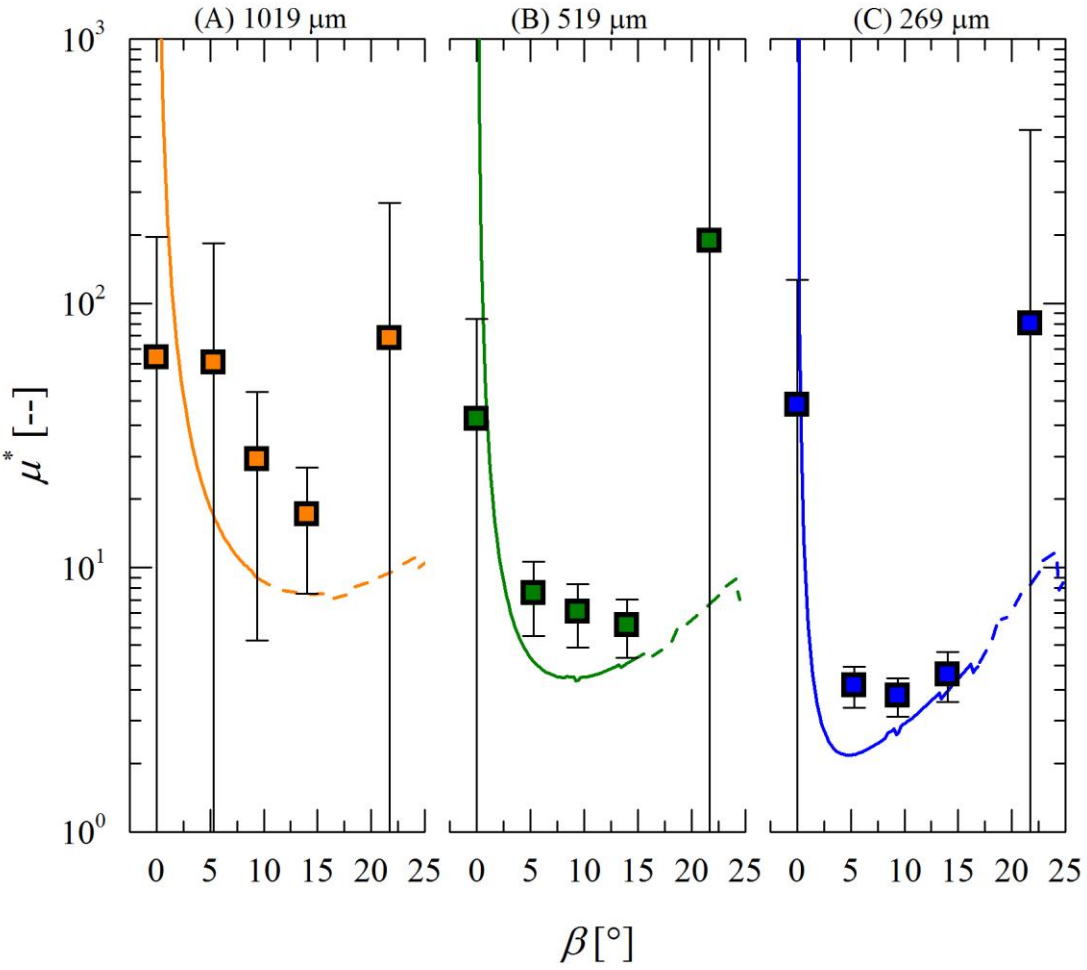

Figure 14: Effective friction coefficient μ^* taken at Ω=10 rad/s (lines are predictions, symbols from experiments of Schuh and Ewoldt [1]). The error bars come from propagation of error for the experimental torque and normal force data (Equation (13)**);** dashed lines indicate predictions outside the applicability range of the Reynolds equation. The optimal texture angle is the minimum of the effective friction coefficient curve, which is dependent on the gap height. Good agreement is seen between the experiments and the simulations where the Reynolds equation is valid.

7 Conclusions

We have developed a computational method for solving the Reynolds equation in cylindrical coordinates using the pseudo-spectral method. We showed that the expected exponential decay in the error is observed when compared to an analytic solution, validating the numerical method. We also showed good agreement between the simulations and experimental data for a flat plate, a symmetric texture, and four asymmetric surface textures at multiple gap heights, and that the deviations between the simulations and experimental data are due to experimental imperfections (asymmetry in bi-directional sliding) and neglecting terms in order to be consistent with the Reynolds equation analysis. Finally, we found that an optimal β exists, dependent on the gap height but not velocity, suggesting an optimal h_0 / D for decreasing friction with asymmetric surface textures.

This validated numerical method serves as a basis for future work on the inverse problem of designing the optimal surface texture profile for decreasing friction in thrust bearings. The optimization studied here was very limited in nature; only one geometrical parameter was changed. However, this numerical method was derived for an arbitrary topography $h = h(r, \theta)$; therefore, this method can be coupled with other optimization tools to determine the best surface texture profile for decreasing friction in thrust bearings with Newtonian fluids. We are already pursing this optimization effort [2].

Acknowledgements

The authors would like to thank Paul Fischer, who taught the basics of the pseudo spectral method that this work is based on. This work was supported by the National Science Foundation under Grant no. CMMI-1463203 and also by the Engineering Research Center for Compact and

Efficient Fluid Power (CCEFP), supported by the National Science Foundation under Grant no. EEC-0540834.

References

[1] J. Schuh and R. Ewoldt, "Asymmetric surface textures decrease friction with Newtonian fluids in full film lubricated sliding contact," *Tribology International,* vol. 97, pp. 490-498, 2016.

[2] Y. Lee, J. Schuh, R. Ewoldt and J. Allison, "Shape parameterization comparison for full-film lubrication texture design," in *ASME 2016 International Design Engineering Technical Conferences, to appear*, Charlotte, NC, USA, 2016.

[3] J. Schuh, "Surface textures and Non-Newtonian fluids for decreased friction in full film lubrication," *Masters Thesis, Department of Mechanical Science and Engineering, University of Illinois at Urbana-Champaign,* 2015.

[4] C. Shen and M. Khonsari, "Effect of dimple's internal structure on hydrodynamic lubrication," *Tribology Letters,* vol. 52, pp. 415-430, 2013.

[5] T. Nanbu, N. Ren, Y. Yasuda, D. Zhu and Q. Wang, "Micro-textures in concentrated conformal-contact lubrication: effects of texture bottom shape and surface relative motion," *Tribology Letters,* vol. 29, pp. 241-252, 2008.

[6] J. Han, L. Fang, J. Sun, Y. Wang, S. Ge and H. Zhu, "Hydrodynamic lubrication of surfaces with asymmetric microdimple," *Tribology Transactions,* no. 54, pp. 607-614, 2011.

[7] G. Stachowiak and A. Bachelor, Engineering Tribology, Elsivier, 2014.

[8] A. Ronen, I. Etsion and Y. Kligerman, "Friction-reducing surface-texturing in reciprocating automotive components," *Tribology Transactions,* vol. 44, no. 3, pp. 359-366, 2001.

[9] R. Siripuram and L. Stephens, "Effect of deterministic asperity geometry on hydrodynamic lubrication," *Journal of Tribology,* vol. 126, pp. 527-534, 2004.

[10] Y. Qiu and M. Khonsari, "On the prediction of cavitation in dimples using a mass-conservative algorithm," *Journal of Tribology,* vol. 131, pp. 041702-1-11, 2009.

[11] M. Qiu and B. Raeymaekers, "The load-carrying capacity and friction coefficient of incompressible textured parallel slider bearings with surface roughness inside the texture features," *Proceedings of the Institution of Mechanical Engineers, Part J: Journal of Engineering Tribology,* vol. 229, no. 547-556, pp. 1-10, 2015.

[12] J. Zhang, L. Su and F. E. Talke, "Effect of surface texture on the flying characteristics of pico sliders," *IEEE Transactions on Magnetics,* vol. 41, pp. 3022-3024, 2005.

[13] S. Kango, D. Singh and R. Sharma, "Numerical investigation on the influence of surface texture on the performance of hydrodynamic journal bearing," *Meccanica,* vol. 47, pp. 469-482, 2012.

[14] N. Tala-Ighil, P. Maspeyrot, M. Fillon and A. Bountif, "Effects of surface texture on journal-bearing characteristics under steady-state operating conditions," *Proceedings of the Institution of Mechanical Engineers, Part J: Journal of Engineering Tribolgoy,* vol. 221, pp. 623-633, 2007.

[15] L. Wang, W. Wang, H. Wang, T. Ma and Y. Hu, "Numerical analysis on the factors affecting the hydrodynamic performance for the parallel surfaces with microtextures," *Journal of Tribology,* vol. 136, pp. 021702-1-8, 2014.

[16] H. Yu, X. Wang and F. Zhou, "Geometric shape effects of surface texture on the generation of hydrodynamic pressure between conformal contacting surfaces," *Tribology Letters,* vol. 37, pp. 123-130, 2010.

[17] M. Dobrica, M. Fillon, M. Pascovici and T. Cicone, "Optimizing surface texture for hydrodynamic lubricated contacts using a mass-conserving numerical approach," *Proceedings of the Institution of Mechanical Engineers, Part J: Journal of Engineering Tribology,* vol. 224, pp. 737-750, 2010.

[18] C. Shen and M. Khonsari, "Numerical optimization of texture shape for parallel surface under unidirectional and bidirectional sliding," *Tribology International,* vol. 82, pp. 1-11, 2015.

[19] M. Wakuda, Y. Yamauchi, S. Kanzaki and Y. Yasuda, "Effect of surface texturing on friction reduction between ceramic and steel materials under lubricated sliding contact," *Wear,* vol. 254, no. 3-4, pp. 356-363, 2003.

[20] Y. Feldman, Y. Kligerman, I. Etsion and S. Haber, "The validity of the Reynolds equation in modeling hydrostatic effects in gas lubricated textured parallel surfaces," *Journal of Tribology,* vol. 128, pp. 345-350, 2006.

[21] M. Qiu, B. Bailey, R. Stoll and B. Raeymaekers, "The accuracy of the compressible Reynolds equation for prediction the local pressure in gas-lubricated textured parallel slider bearing," *Tribology International,* vol. 72, pp. 83-89, 2014.

[22] T. Woloszynski, P. Podsiadlo and G. Stachowiak, "Evaluation of discretization and integration methods for the analysis of hydrodynamic bearings with and without surface texturing," *Tribology Letters,* vol. 51, pp. 25-47, 2013.

[23] M. Dobrica and M. Fillon, "About the validity of Reynolds equation and inertia effects in textured sliders of infinite width," *Proceedings of the Institution of Mechanical Engineers, Part J: Journal of Engineering Tribology,* vol. 223, pp. 69-78, 2009.

[24] G. Jang, S. Lee and H. Kim, "Finite element analysis of the coupled journal and thrust bearing in a computer hard disk drive," *Journal of Tribology,* vol. 128, pp. 335-340, 2006.

[25] M. E. Wahl and F. E. Talke, "Numerical simulation of the steady state flying characteristics of a 50% slider with surface texture," *IEEE Transactions on Magnetics,* vol. 30, pp. 4122-4124, 1994.

[26] M. Schumack, "Application of the psuedospectral method to thermohydrodynamic lubrication," *International Journal for Numerical Methods in Fluids,* vol. 23, pp. 1145-1161, 1996.

[27] S. Gantasala, I. R. P. Krishna and A. S. Sekhar, "Dynamic analysis of rotors supported on journal bearings by solving Reynolds equation using pseudospectral method," in *Proceedings of the 9th IFToMM International Conference on Rotor Dynamics*, 2015.

[28] M. Hussaini and T. Zang, "Spectral methods in fluid dynamics," *Annual Review of Fluid Mechancis,* vol. 19, pp. 339-367, 1987.

[29] B. Fornberg and D. Sloan, "A review of pseudo spectral methods for solving partial differential equations," *Acta Numerica,* vol. 3, pp. 203-267, 1994.

[30] J. Shen, "Efficient spectral-galerkin method I. Direct solvers of second- and fourth-order euqations using Legendre polynomials," *SIAM Journal of Scientific Computing,* vol. 15, pp. 1489-1505, 1994.

[31] M. Heath, Scientific Computing: An Introductory Survey, 2nd Edition ed., McGraw-Hill, 2002.

[32] K. E. Beschorner, C. F. Higgs III and M. R. Lovell, "Derivation of Reynolds equation in cylindrical coordinates applicable to pin-on-disk and cmp," in *Proceedings of the STLE/ASME International Joint Tribology Conference*, Miami, FL, USA, 2008.

[33] H. Lewis and P. Bellan, "Physical constraints on the coefficients of Fourier expansions in cylindrical coordinates," *Journal of Mathematical Physics,* vol. 31, no. 11, pp. 2592-2596, 1990.

[34] G. Karniadakis and S. Sherwin, Spectral/hp Element Methods for Computational Fluid Dynamics, Oxford University Press, 2005.

[35] D. Kopriva, Implementing Spectral Methods for Partial Differential Equations, Springer, 2009.

[36] B. Fornberg, A Practical Guide to Pseudospectral Methods, Cambridge: Cambridge University Press, 1998.

[37] M. Deville, P. Fischer and E. Mund, High-Order Methods for Incompressible Fluid Flow, Cambridge University Press, 2002.

[38] G. Strang, Computational Science and Engineering, Wellesley-Cambridge, 2007.

[39] L. Meirovitch, Fundamental of Vibrations, Waveland Press, Inc., 2010.

[40] M. Fesanghary and M. Khonsari, "On the optimum groove shapes for load-carrying capacity enhancement in parallel flat surface bearings: Theory and experiment," *Tribology International,* vol. 67, pp. 254-262, 2013.

[41] Macosko, Rheology: Principles, Measurements, and Applications, Wiley-VCH, 1994.

[42] O. Reynolds, "On the theory of lubrication and its application to Mr. Beauchamp Tower's experiments including an experimental determination of the viscosity of olive oil," *Philosophical Transactions of the Royal Society of London,* vol. 177, pp. 157-234, 1886.

[43] L. Rayleigh, "Notes on the theory of lubrication," *The London, Edinburgh, and Dublin Philosophical Magazine and Journal of Science,* no. 35, pp. 1-12, 1918.

Supplemental Information for:

Design-driven modeling of surface-textured full-film lubricated sliding: validation and rationale of non-standard thrust observations

Jonathon K. Schuh[1], Yong Hoon Lee[1],
James T. Allison[2], Randy H. Ewoldt[1]*

[1]*Department of Mechanical Science and Engineering*
University of Illinois at Urbana-Champaign, Urbana, Illinois 61801
[2]*Department of Industrial Enterprise and Systems Engineering*
University of Illinois at Urbana-Champaign, Urbana, Illinois 61801

Governing Equation

The Reynolds equation in cylindrical coordinates is derived from mass conservation for an incompressible fluid and the Navier-Stokes (conservation of momentum) equations in cylindrical coordinates [1], given as

$$\frac{1}{r}\frac{\partial}{\partial r}\left(rv_r\right)+\frac{1}{r}\frac{\partial v_\theta}{\partial \theta}+\frac{\partial v_z}{\partial z}=0 \tag{1}$$

$$\begin{aligned}
\rho\left(\frac{Dv_r}{Dt}\right)&=-\frac{\partial p}{\partial r}+\eta\left[\frac{\partial}{\partial r}\left(\frac{1}{r}\frac{\partial}{\partial r}\left(rv_r\right)\right)+\frac{1}{r^2}\frac{\partial^2 v_r}{\partial \theta^2}+\frac{\partial^2 v_r}{\partial z^2}-\frac{2}{r^2}\frac{\partial v_\theta}{\partial \theta}\right]\\
\rho\left(\frac{Dv_\theta}{Dt}\right)&=-\frac{1}{r}\frac{\partial p}{\partial \theta}+\eta\left[\frac{\partial}{\partial r}\left(\frac{1}{r}\frac{\partial}{\partial r}\left(rv_\theta\right)\right)+\frac{1}{r^2}\frac{\partial^2 v_\theta}{\partial \theta^2}+\frac{\partial^2 v_\theta}{\partial z^2}+\frac{2}{r^2}\frac{\partial v_r}{\partial \theta}\right]\\
\rho\left(\frac{Dv_z}{Dt}\right)&=-\frac{\partial p}{\partial z}+\eta\left[\frac{1}{r}\frac{\partial}{\partial r}\left(r\frac{\partial v_z}{\partial r}\right)+\frac{1}{r^2}\frac{\partial^2 v_z}{\partial \theta^2}+\frac{\partial^2 v_z}{\partial z^2}\right]
\end{aligned} \tag{2}$$

where ρ is the fluid density, p is the pressure, η is the fluid viscosity, $v_r\left(r,\theta,z\right)$ is the r velocity component, $v_\theta\left(r,\theta,z\right)$ is the θ velocity component, $v_z\left(r,\theta,z\right)$ is the z velocity component, and $\frac{D}{Dt}$ is the material derivative, which in cylindrical coordinates is

$$\begin{aligned}
\frac{Dv_r}{Dt} &= \frac{\partial v_r}{\partial t} + v_r \frac{\partial v_r}{\partial r} + \frac{v_\theta}{r}\frac{\partial v_r}{\partial \theta} - \frac{v_\theta^{\,2}}{r} + v_z \frac{\partial v_r}{\partial z} \\
\frac{Dv_\theta}{Dt} &= \frac{\partial v_\theta}{\partial t} + v_r \frac{\partial v_\theta}{\partial r} + \frac{v_\theta}{r}\frac{\partial v_\theta}{\partial \theta} + \frac{v_r v_\theta}{r} + v_z \frac{\partial v_\theta}{\partial z} \\
\frac{Dv_z}{Dt} &= \frac{\partial v_z}{\partial t} + v_r \frac{\partial v_z}{\partial r} + \frac{v_\theta}{r}\frac{\partial v_z}{\partial \theta} + v_z \frac{\partial v_z}{\partial z}.
\end{aligned} \tag{3}$$

Equation (2) can be simplified by making the following assumptions:

1) Inertial terms are negligible
2) $h_0 / R \to 0$ where h_0 is the reference gap height and *R* is the reference radius
3) The pressure is invariant in the *z* direction
4) The fluid is an isoviscous Newtonian fluid

The simplified Navier-Stokes equations then become a balance of pressure and viscous forces given by

$$\begin{aligned}
\frac{\partial p}{\partial r} &= \eta \frac{\partial^2 v_r}{\partial z^2} \\
\frac{1}{r}\frac{\partial p}{\partial \theta} &= \eta \frac{\partial^2 v_\theta}{\partial z^2}
\end{aligned} \tag{4}$$

and the conservation of mass equation is the same as Equation (1).

The velocity boundary conditions used are

$$\begin{aligned}
&\text{at } z=0\text{: } v_\theta = r\Omega \text{ and } v_r = v_z = 0 \\
&\text{at } z = h\text{: } v_\theta = v_r = v_z = 0
\end{aligned} \tag{5}$$

where Ω is the prescribed angular velocity of the flat plate and $h(r,\theta)$ is the gap height, which can be a function of both *r* and θ.

Solving Equation (4) through direct integration with respect to *z* and by applying the boundary conditions given in Equation (5) gives

$$v_r = \frac{1}{2\eta}\frac{\partial p}{\partial r}\left(z^2 - zh\right)$$
$$v_\theta = \frac{1}{2\eta}\frac{1}{r}\frac{\partial p}{\partial \theta}\left(z^2 - zh\right) + r\Omega\left(\frac{h-z}{h}\right). \tag{6}$$

It can be seen from Equation (6) that v_θ is a linear combination of both simple shear flow (Couette drag flow) and pressure driven flow (Poiseuille flow) and v_r involves only pressure driven flow. Substituting Equation (6) into the continuity equation (Equation (1)), integrating in the *z* direction to remove *z* dependence, and applying Liebnitz's integration rule gives the Reynolds equation in cylindrical coordinates as

$$\frac{1}{r}\frac{\partial}{\partial r}\left(rh^3\frac{\partial p}{\partial r}\right) + \frac{1}{r}\frac{\partial}{\partial \theta}\left(\frac{h^3}{r}\frac{\partial p}{\partial \theta}\right) = 6\eta\Omega\frac{\partial h}{\partial \theta} + 12\eta\frac{\partial h}{\partial t}. \tag{7}$$

If the system is assumed to be in steady state, then the steady form of the Reynolds equation in cylindrical coordinates is

$$\frac{1}{r}\frac{\partial}{\partial r}\left(rh^3\frac{\partial p}{\partial r}\right) + \frac{1}{r}\frac{\partial}{\partial \theta}\left(\frac{h^3}{r}\frac{\partial p}{\partial \theta}\right) = 6\eta\Omega\frac{\partial h}{\partial \theta} \tag{8}$$

which is an elliptic, non-constant coefficient, second order partial differential equation for the pressure field $p(r,\theta)$. If the gap height $h\left(r,\theta\right)$ is prescribed (and boundary conditions for the pressure in the *r* and θ directions are also prescribed) then Equation (8) can be solved explicitly for the pressure and used in Equation (6) to calculate the velocity field.

Comparison of Numerical Methods

Several numerical methods can be used to solve the steady Reynolds equation, Equation (8). We use the pseudo-spectral method because it guarantees that the pressure solution is continuous, differentiable, and integrable [2], which is important because we want to compare the

normal force (integral of pressure) and shear stress (from derivatives of velocity, and thus derivatives of pressure) from simulations to experiments.

The most popular method for solving the Reynolds equation with surface textures has been the finite difference method (FDM) [3, 4, 5, 6, 7, 8, 9, 10, 11, 12]. The resulting matrices are sparse because the differences are defined with respect to the nearest nodal points. However, the solution method using FDM is not guaranteed to be continuous, differentiable, or integrable, since FDM only acts on the function at the specified grid points [2]. It can also be shown through a Taylor series expansion that the error ε between the true solution and the computed solution decays as

$$\varepsilon \sim \frac{1}{N^a} \tag{9}$$

where N is the number of grid points in an equally spaced mesh and a is the convergence rate that depends on the type of FDM used; a=1 for Euler-Forward/Euler-Backward, a=2 for Central Finite Differences, and a>2 for higher order differencing schemes. Therefore, a large number of grid points may be needed to decrease the error between the true solution and the computed solution, resulting in a large computational cost.

The finite volume method (FVM) has also been used [12, 13], and the results can be better than those obtained by FDM since FVM is a conservative method (the efflux out from one control volume is the influx into the neighboring control volumes). The matrices produced using FVM are also sparse, since each control volume interacts only with its nearest neighbors [14]. However, the solution using FVM cannot be guaranteed to be continuous, differentiable, or integrable, since FVM only acts at discrete points (usually the centers of the control volumes). The error between the true solution and the computed solution also decays in the same way as that given in Equation (9), meaning a large number of control volumes is needed to decrease the error, resulting in a large computational cost.

One method to avoid the problems associated with FDM and FVM is to use the finite element method (FEM) [12, 15, 16]. The resulting solution is guaranteed to be continuous and integrable (though not differentiable), since FEM operates on coefficients of basis functions instead of discrete functional points [2, 17]. The resulting matrices are still sparse, since the basis functions are defined to be non-zero locally. The error between the true solution and the computed solution decays in the same way as Equation (9), where a=4 for piecewise linear finite elements.

A method that is guaranteed to be continuous, integrable, *and differentiable* is the spectral/pseudo-spectral method [12, 18, 19]. In this method, the basis functions are smooth, continuous functions that are defined over the entire domain [17, 20]. The error ε between the true solution and the computed solution decays as [21, 22, 23]

$$\varepsilon \sim \frac{1}{e^N} \tag{10}$$

where N is the number of grid points. It should be noted that the resulting matrices are no longer sparse, because the basis functions are defined over the entire domain. However, since the error between the true solution and the computed solution converges exponentially in space, a small number of grid points are needed to reduce the error, resulting in a small computational cost. Therefore, since the computational cost is small, and the solution is continuous, differentiable, and integrable, we use the pseudo-spectral method.

Formulation and Solution Procedure

We write our own code for using the pseudo-spectral method to solve Equation (8) for the pressure so that it can be coupled to optimization tools (for optimization studies outside the scope of the work presented here [24]). The pseudo-spectral method solves the governing partial

differential equation using a weighted residual technique (WRT) that computes an approximate solution to the differential equation [2, 17, 20].

We apply the WRT to Equation (8) by multiplying by a test function w and integrating over the computational domain (Figure 3) which yields the weak form of the Reynolds Equation

$$\int_{-\varphi/2}^{\varphi/2}\int_{R_i}^{R_o} w\frac{1}{r}\frac{\partial}{\partial r}\left(rh^3\frac{\partial p}{\partial r}\right)drd\theta+\int_{-\varphi/2}^{\varphi/2}\int_{R_i}^{R_o} w\frac{1}{r}\frac{\partial}{\partial \theta}\left(\frac{h^3}{r}\frac{\partial p}{\partial \theta}\right)drd\theta=\int_{-\varphi/2}^{\varphi/2}\int_{R_i}^{R_o} w6\eta\Omega\frac{\partial h}{\partial \theta}drd\theta \quad (11)$$

where φ is the span in the θ direction and $\varphi = 2\pi / N_{tex}$ where N_{tex} is the number of periodic "pie" slices and R_i and R_o are the inner and outer radii respectively. This can be simplified using integration by parts to reduce the degree of differentiability on the left hand side [2, 17, 20] and using appropriate boundary conditions given in the main body of the text to obtain

$$-\int_{-\varphi/2}^{\varphi/2}\int_{R_i}^{R_o}\left(\frac{\partial w}{\partial r}rh^3\frac{\partial p}{\partial r}+\frac{\partial w}{\partial \theta}\frac{h^3}{r}\frac{\partial p}{\partial \theta}\right)drd\theta=6\eta\Omega\int_{-\varphi/2}^{\varphi/2}\int_{R_i}^{R_o} wr\frac{\partial h}{\partial \theta}drd\theta. \quad (12)$$

The integrals in Equation (12) will be solved numerically. We use Gauss-Lobatto-Legendre quadrature to evaluate the integrals. In this quadrature rule, the quadrature evaluations occur over a domain [-1, 1]. The interior discretized points are located at the zeros of the derivative of the Nth order Legendre polynomial [25], resulting in N+1 total mesh points. The quadrature weights are optimally chosen so that the quadrature is exact for polynomials of degree 2N-1 [2]. Since our quadrature evaluation points occur over the domain [-1,1], a change of variables must be performed to evaluate the integrals. The new variables, with domain [-1,1] are given as

$$\xi=\frac{2}{R_o-R_i}\left(r-\frac{R_o+R_i}{2}\right)$$
$$\psi=\frac{2}{\varphi}\theta. \quad (13)$$

Using Equation (13) to change variables in Equation (12) gives

$$
\begin{aligned}
&-\frac{\varphi}{R_o-R_i}\int_{-1}^{1}\int_{-1}^{1}\frac{\partial w}{\partial \xi}r(\xi)h^3\frac{\partial p}{\partial \xi}d\xi d\psi \\
&-\frac{R_o-R_i}{\varphi}\int_{-1}^{1}\int_{-1}^{1}\frac{\partial w}{\partial \psi}\frac{h^3}{r(\xi)}\frac{\partial p}{\partial \psi}d\xi d\psi \\
&=3\eta\Omega(R_o-R_i)\int_{-1}^{1}\int_{-1}^{1}wr(\xi)\frac{\partial h}{\partial \psi}d\xi d\psi.
\end{aligned}
\tag{14}
$$

Finally, the pseudo-spectral method assumes that the functions *w* and *p* can be written as linear combinations of basis functions. If the Galerkin method is used, then the basis functions for *w* and *p* are the same [2, 17, 20] and *w* and *p* can be written as

$$
\begin{aligned}
w&=\sum_{i=1}^{N+1}\sum_{j=1}^{N+1}w_{ij}\rho_i(\xi)\rho_j(\psi) \\
p&=\sum_{l=1}^{N+1}\sum_{m=1}^{N+1}p_{lm}\rho_l(\xi)\rho_m(\psi)
\end{aligned}
\tag{15}
$$

where ρ is the basis function in one dimension and w_{ij} and p_{lm} are the coefficients of the basis functions. As basis functions, we chose Nth order Lagrange polynomials

$$
\rho_i(x)=\prod_{\substack{1\le j\le N+1\\ j\neq i}}\frac{(x-x_j)}{(x_i-x_j)}
\tag{16}
$$

where x_i and x_j are the grid point locations, i.e. the Gauss-Lobatto-Legendre points. Example basis functions are given in Figure S1. We selected these basis functions because $\rho_i(x_j)=\delta_{ij}$, where δ_{ij} is the Kronecker delta, which simplifies the numerical evaluation of the integrals in Equation (14), and also means that the coefficients p_{lm} correspond to the pressure evaluated at the grid points.

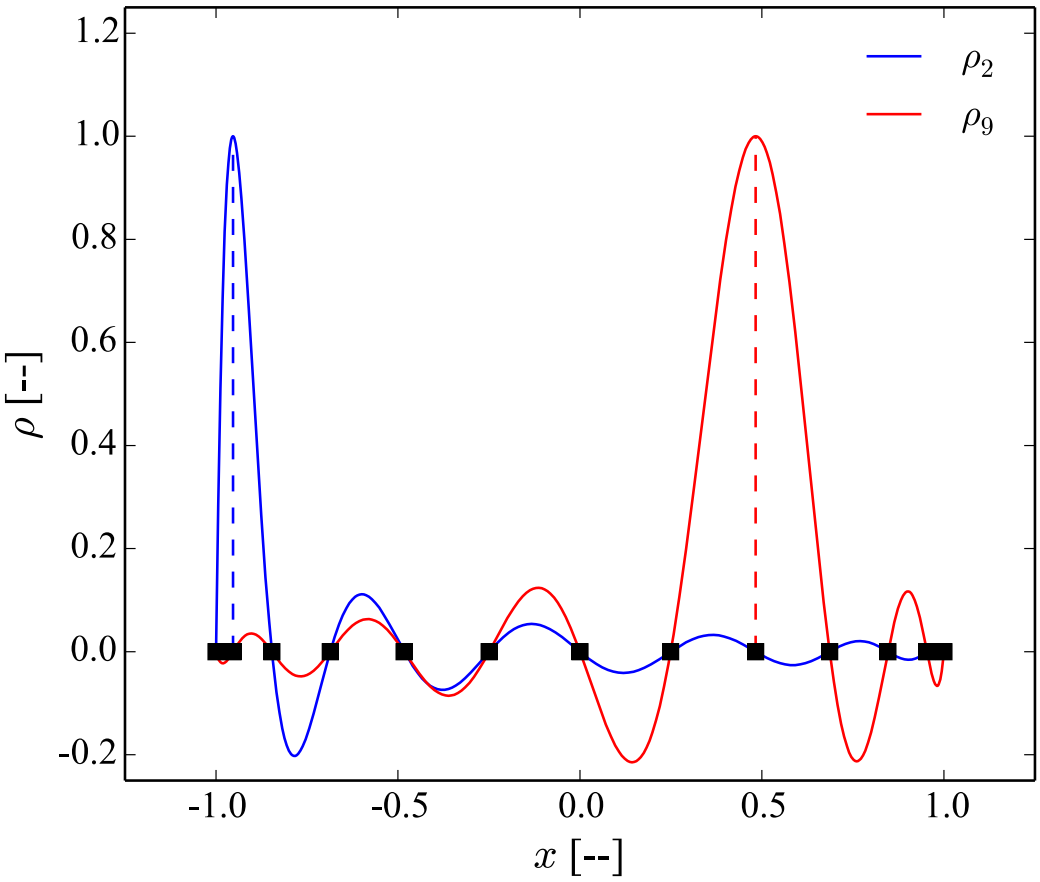

Figure S1: Example N=12 order Lagrange polynomial basis functions for i=2 and i=9 (Equation (16)). We use N=65 order in the pseudo-spectral method to solve the Reynolds equation.

Substituting Equation (15) into Equation (14) gives

$$\begin{aligned}
&\left(\sum_{i,j=1}^{N+1}\sum_{l,m=1}^{N+1} w_{ij}\left[-\frac{\varphi}{R_o-R_i}\int_{-1}^{1}\int_{-1}^{1}\frac{d\rho_i}{d\xi}\rho_j r(\xi)h^3\frac{d\rho_l}{d\xi}\rho_m d\xi d\psi\right]p_{lm}\right)\\
&+\left(\sum_{i,j=1}^{N+1}\sum_{l,m=1}^{N+1} w_{ij}\left[-\frac{R_o-R_i}{\varphi}\int_{-1}^{1}\int_{-1}^{1}\rho_i\frac{d\rho_j}{d\psi}\frac{h^3}{r(\xi)}\rho_l\frac{d\rho_m}{d\psi}d\xi d\psi\right]p_{lm}\right)\\
&=\left(\sum_{i,j=1}^{N+1} w_{ij}\left[3\eta\Omega(R_o-R_i)\int_{-1}^{1}\int_{-1}^{1}\rho_i\rho_j r(\xi)\frac{\partial h}{\partial\psi}d\xi d\psi\right]\right).
\end{aligned} \tag{17}$$

It can be seen that Equation (17) can be written in matrix form as

$$\underline{w}^T K\underline{p} = \underline{w}^T\,\underline{f} \tag{18}$$

which is a linear system of equations where $\underline{w}$ and $\underline{p}$ are the vectors containing the coefficients, K is a matrix defined as

$$\begin{aligned} K_{ijlm} = &-\frac{\varphi}{R_o - R_i}\int_{-1}^{1}\int_{-1}^{1}\frac{d\rho_i}{d\xi}\rho_j r(\xi)h^3\frac{d\rho_l}{d\xi}\rho_m d\xi d\psi \\ &-\frac{R_o - R_i}{\varphi}\int_{-1}^{1}\int_{-1}^{1}\rho_i\frac{d\rho_j}{d\psi}\frac{h^3}{r(\xi)}\rho_l\frac{d\rho_m}{d\psi}d\xi d\psi, \end{aligned} \tag{19}$$

and $\underline{f}$ is a vector defined as

$$f_{ij} = 3\eta\Omega(R_o - R_i)\int_{-1}^{1}\int_{-1}^{1}\rho_i\rho_j r(\xi)\frac{\partial h}{\partial\psi}d\xi d\psi. \tag{20}$$

It should be noted that K is a symmetric matrix and depends only on the 1st derivatives of the basis functions [2]; this is a direct result of using the integration by parts in Equation (12). We also assumed that the gap (texture) topography h could also be written as

$$h = \sum_{a=1}^{N+1}\sum_{b=1}^{N+1}h_{ab}\rho_a(\xi)\rho_b(\psi). \tag{21}$$

where h_{ab} is the gap height evaluated at the grid points.

Using the Gauss-Lobatto-Legendre quadrature rule for evaluating the integrals defining K and $\underline{f}$ yields K and $\underline{f}$ in matrix form as [26]

$$\begin{aligned} K = &-\frac{\varphi}{R_o - R_i}(I\otimes D)^T(M\otimes M)(I\otimes R)H^3(I\otimes D) \\ &-\frac{R_o - R_i}{\varphi}(D\otimes I)^T(M\otimes M)(I\otimes R^{-1})H^3(D\otimes I) \end{aligned} \tag{22}$$

$$\underline{f} = 3\eta\Omega(R_o - R_i)(M\otimes M)(I\otimes R)(D\otimes I)\underline{h} \tag{23}$$

where M is a diagonal matrix containing the quadrature weights, D is a full matrix such that $\frac{\partial\rho_i}{\partial x}|_{x_j} \approx D\underline{\rho}_i$ [25], R is a diagonal matrix containing the values of r from R_i to R_o, H is a diagonal

matrix containing the values of h at the grid points, I is the identity matrix, $\underline{h}$ is a vector containing the gap height evaluated at the quadrature points, and $\otimes$ specifies the Kronecker tensor product allowing matrices in 1-D to be extended to higher space dimensions [26].

The above analysis is true for every grid point in the computational domain, resulting in a system of $(N+1)^2$ equations that need to be solved. We can reduce the number of equations by imposing the boundary conditions using [27, 28]

$$\begin{aligned} \underline{w} &= B\underline{w}' \\ \underline{p} &= B\underline{p}' \end{aligned} \tag{24}$$

where $\underline{w}'$ and $\underline{p}'$ are the vectors containing the coefficients at the interior nodes and the matrix $B = B_\psi \otimes B_\xi$, where B_ψ defines the boundary conditions in the ψ direction and B_ξ defines the boundary conditions in the ξ direction. Examples of B_ξ and B_ψ are given in subsequent sections because the exact structure of the matrices are problem specific. Substituting Equation (24) into Equation (18) gives

$$\underline{w}'^T B^T K B \underline{p}' = \underline{w}'^T B^T \underline{f} \tag{25}$$

which can be rewritten as

$$\underline{w}'^T K' \underline{p}' = \underline{w}'^T \underline{f}' \tag{26}$$

where

$$\begin{aligned} K' &= B^T K B \\ \underline{f}' &= B^T \underline{f}. \end{aligned} \tag{27}$$

For non-trivial solutions, Equation (26) can be rewritten as find $\underline{p}'$ such that

$$K'\underline{p}' = \underline{f}' \tag{28}$$

which eliminates the need to solve for the test function w. Since K' and $\underline{f}'$ are already known from Equations (22), (23), and (27) for a given $h(r,\theta)$, Ω, and boundary conditions, Equation (28) can be inverted to obtain $\underline{p}'$ directly. The full solution $\underline{p}$ that satisfies the boundary conditions can then be obtained from Equation (24).

The full pressure solution will be used to calculate the normal force of the flat plate through an integration of the pressure over the area, calculated as

$$F_N = \int_0^{2\pi} \int_{R_i}^{R_o} p r dr d\theta, \tag{29}$$

and it can be seen that since inertial effects are negligible, normal force is proportional to viscosity and rotation speed

$$F_N \sim \eta\Omega. \tag{30}$$

Derivatives of pressure are used to determine the velocity field through Equation (6), and derivatives of velocity components determine the shear stress on the top plate

$$\tau_{\theta z}|_{z=0} = \eta\left(\frac{1}{r}\frac{\partial v_z}{\partial \theta} + \frac{\partial v_\theta}{\partial z}\right)|_{z=0}. \tag{31}$$

This is integrated to calculate the total shear load in terms of torque

$$M = \int_0^{2\pi} \int_{R_i}^{R_o} \left(r\tau_{\theta z}|_{z=0}\right) r dr d\theta, \tag{32}$$

and it can again be seen that the load scales linearly with viscosity and rotation speed

$$M \sim \eta\Omega. \tag{33}$$

Using the torque and the normal force, we define an effective friction coefficient μ^*, similar to previous work [29], as

$$\mu^* \equiv \frac{M / R}{F_N} \tag{34}$$

which is independent of the fluid viscosity or speed of rotation and only depends on the texture gap height profile.

Comparison to Analytic Solution

To verify the solution method outlined in the previous section, the numerical solution is compared to an analytic solution of the Reynolds equation in cylindrical coordinates. The analytic solution is obtained in the limit that $R_o - R_i << 1,$ causing the pressure to not vary in the *r* direction, and that $h = h(\theta)$ only, which will be specified. These assumptions allow Equation (8) to be rewritten as

$$\frac{1}{r}\frac{d}{d\theta}\left(\frac{h^3}{r}\frac{dp}{d\theta}\right) = 6\eta\Omega\frac{dh}{d\theta}. \tag{35}$$

We choose to specify the gap height as a linearly varying function

$$h = \frac{h_1 - h_0}{\varphi}\theta + \frac{h_1 + h_0}{2} \tag{36}$$

where φ is the total span in the θ direction, $h(\theta = \varphi/2) = h_1$, and $h(\theta = -\varphi/2) = h_0$. This gap height profile was selected because it is smooth and it allows an analytical solution to the Reynolds equation. We choose the boundary conditions

$$p(\theta = -\varphi/2) = p(\theta = \varphi/2) = 0. \tag{37}$$

Solving Equation (35) for the pressure as a function of *h* with the given boundary conditions and *h* profile gives

$$p(h)=\frac{6\eta\Omega\varphi r^2}{(h_1-h_0)}\left(-\frac{1}{h}+\frac{h_0h_1}{(h_0+h_1)h^2}+\frac{1}{h_0}\left(1-\frac{h_1}{h_0+h_1}\right)\right) \tag{38}$$

which can be solved for $p(\theta)$ by substituting in Equation (36). The r term in Equation (38) can be treated as a constant, because $\Delta r << 1$. Moreover, the approximately constant value of r sets the velocity $V=r\Omega$ and the distance $L=r\varphi$ in the flow direction, thus the term in the numerator $\Omega\varphi r^2 = VL$. The normal force acting on the flat plate is obtained by integrating in both the θ and r directions: $F_{true} = \int_{-\varphi/2}^{\varphi/2}\int_{R_i}^{R_o} prdrd\theta$, which upon integration gives

$$F_{true}=\frac{3}{2}\eta\Omega R_o{}^2\left(\frac{R_o\varphi}{h_1}\right)^2\frac{\left(1-\left(\frac{R_i}{R_o}\right)^4\right)}{(1-\kappa)^2}\left(\ln(\kappa)+2\left(\frac{1-\kappa}{1+\kappa}\right)\right) \tag{39}$$

where $\kappa=\frac{h_o}{h_1}$. The true normal force is the metric to which the numerical simulations are compared.

The numerical solution is obtained by solving Equation (28) with appropriate boundary conditions. The applied boundary conditions are

$$p(\theta=-\varphi/2)=p(\theta=\varphi/2)=0, \qquad \frac{\partial p}{\partial r}|_{r=R_i}=\frac{\partial p}{\partial r}|_{r=R_o}=0 \tag{40}$$

which are implemented numerically through B_ψ and B_ξ as

$$B_\psi=\begin{bmatrix}0 & 0 & \dots & 0\\ 1 & 0 & \dots & 0\\ | & | & | & |\\ 0 & 0 & \dots & 1\\ 0 & 0 & 0 & 0\end{bmatrix}$$
$$B_\xi = I. \tag{41}$$

The boundary condition in the *r* direction must be specified because numerically we are using the original 2-D form of the steady state Reynolds equation given in Equation (8) and not the simplified 1-D form given in Equation (35). The normal force on the flat plate in obtained using Gauss-Lobatto-Legendre quadrature on the computed pressure by $F_{comp} = \int_{-\varphi/2}^{\varphi/2} \int_{R_i}^{R_o} p_{comp} r dr d\theta$, where p_{comp} is the computed pressure. The error between the computed normal force and the true normal force is calculated as

$$\varepsilon = \frac{|F_{true} - F_{comp}|}{|F_{true}|}. \tag{42}$$

The expected exponential decay in the error is observed [21, 22, 23], validating the numerical method. To verify the predictive capabilities, we compare to experiments with textured disks.

Textured Disk Modeling

In our previously measured experimental results for a surface textured thrust bearing [29], the surface textures are cylindrical holes cut at an angle β, which creates an elliptical top profile. We model our surface textures with an elliptical top profile, similar to the experiments. Figure 3 shows the geometric quantities used to define the surface textures; the finite inner radius is needed so that the $1/r$ terms in Equation (19) do not diverge. Figure S2 shows the convergence of the normal force as the inner radius becomes smaller, and is shown to converge when R_i<0.02 mm (R_i/R_o<0.1%). The geometric values for all the simulated textures are given in Table 1. Examples of the simulated texture surfaces are given in Figure 5.

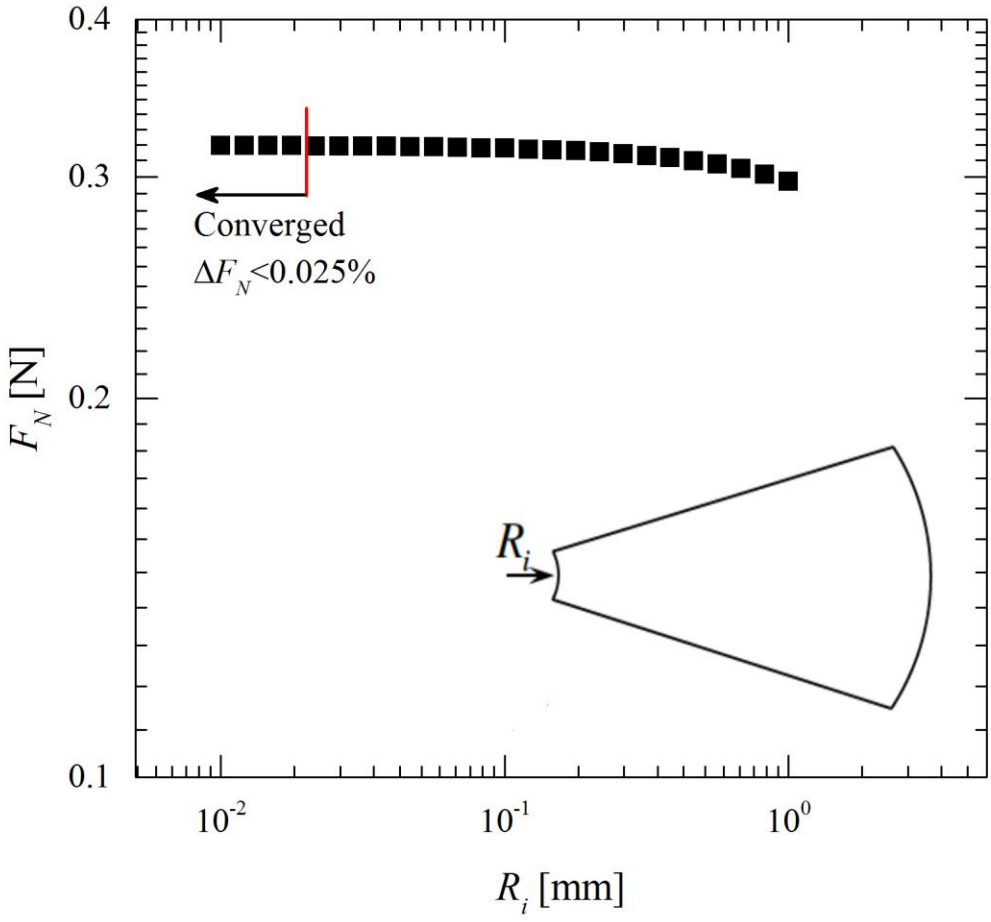

Figure S2: Convergence of the normal force as a function of R_i. The normal force has converged to within 0.025% when R_i< 0.02 mm.

Results for Textured Disks

Pressure and velocity fields were obtained for all the different surface textures tested. Figure S3 is velocity and pressure fields obtained for the flat plate. Figures S4-S6 are velocity and pressure fields obtain with asymmetric textures with β=9.4°, 14°, and 21.7° respectively. Figure S7 is velocity and pressure fields obtained with the symmetric surface texture. The flat plate and β=9.4° and 14° all fall within the regions of applicability given in Figure 7, while β=21.7° and the symmetric texture are outside the applicability region.

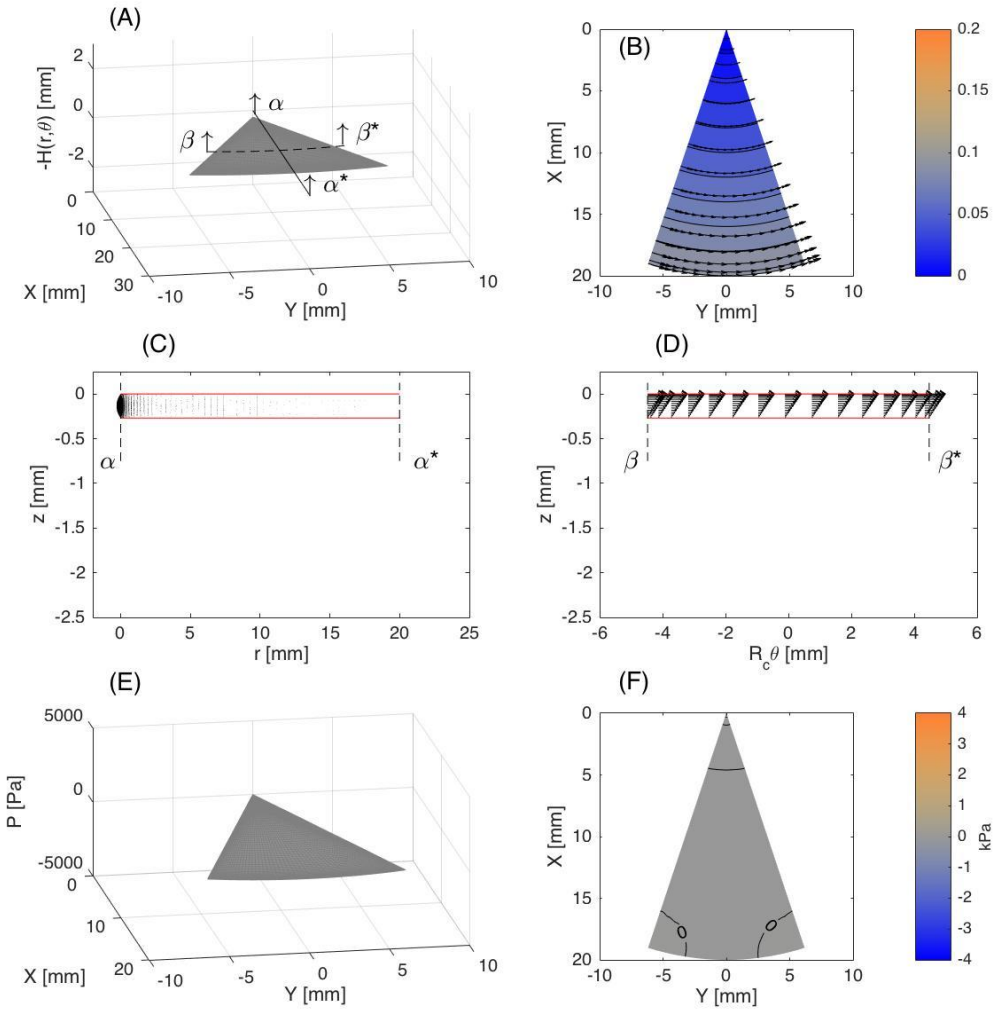

Figure S3: Example computed fields obtained with the Reynolds equation for a flat plate with Ω=10 rad/s at h_0=269 μm, which fall within the regions of applicability given in Figure 7. These computed fields were obtained for each texture tested with input values given in Table 2. (A) surface texture profile, plotted as -h. (B) plot of the velocity field at $z=h_0/2$. (C) velocity field of v_r and v_z at θ=0°. (D) velocity field of v_θ and v_z at $r=R_t$. (E) computed pressure profile. (F) contour of pressure.

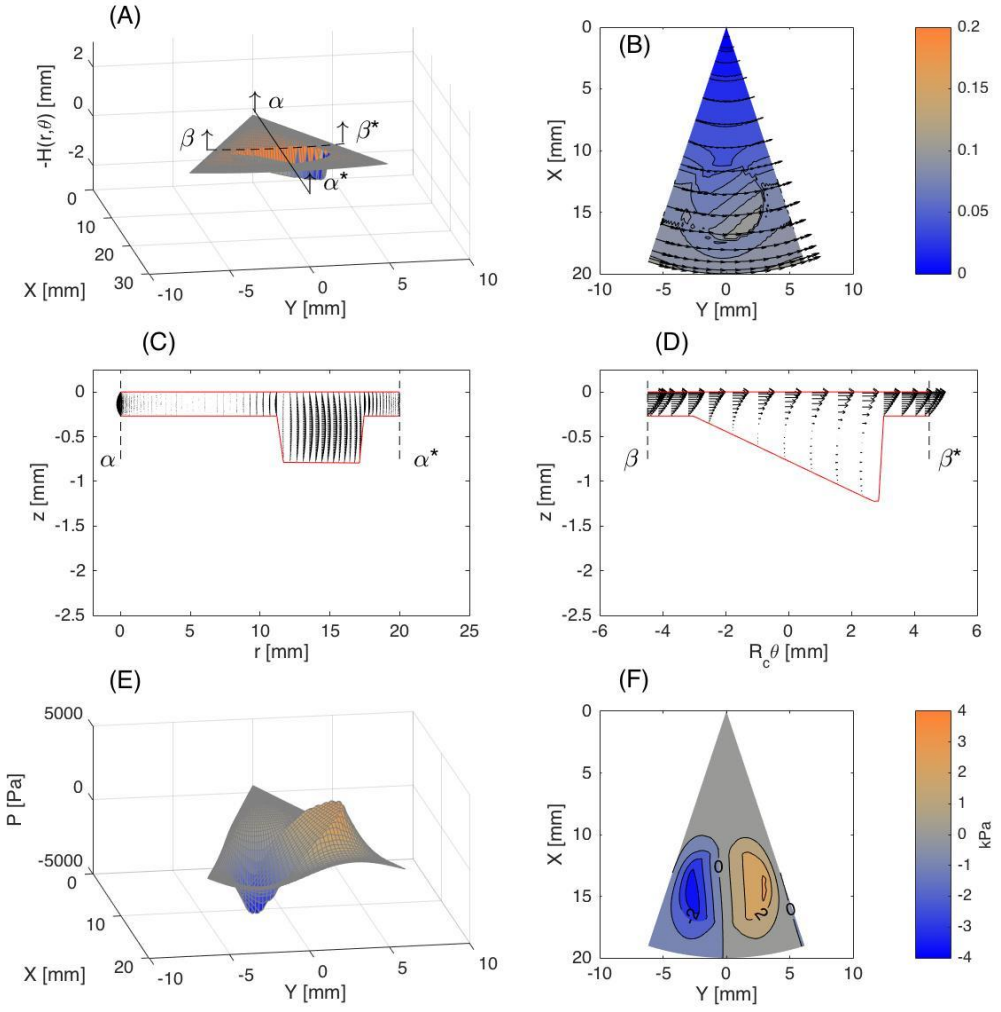

Figure S4: Example computed fields obtained with the Reynolds equation for an asymmetric surface texture with β=9.4° and Ω=10 rad/s at h_0=269 μm, which fall within the regions of applicability given in Figure 7. These computed fields were obtained for each texture tested with input values given in Table 2. (A) surface texture profile, plotted as -h. (B) plot of the velocity field at $z=h_0/2$. (C) velocity field of v_r and v_z at θ=0°. (D) velocity field of v_θ and v_z at $r=R_t$. (E) computed pressure profile. (F) contour of pressure.

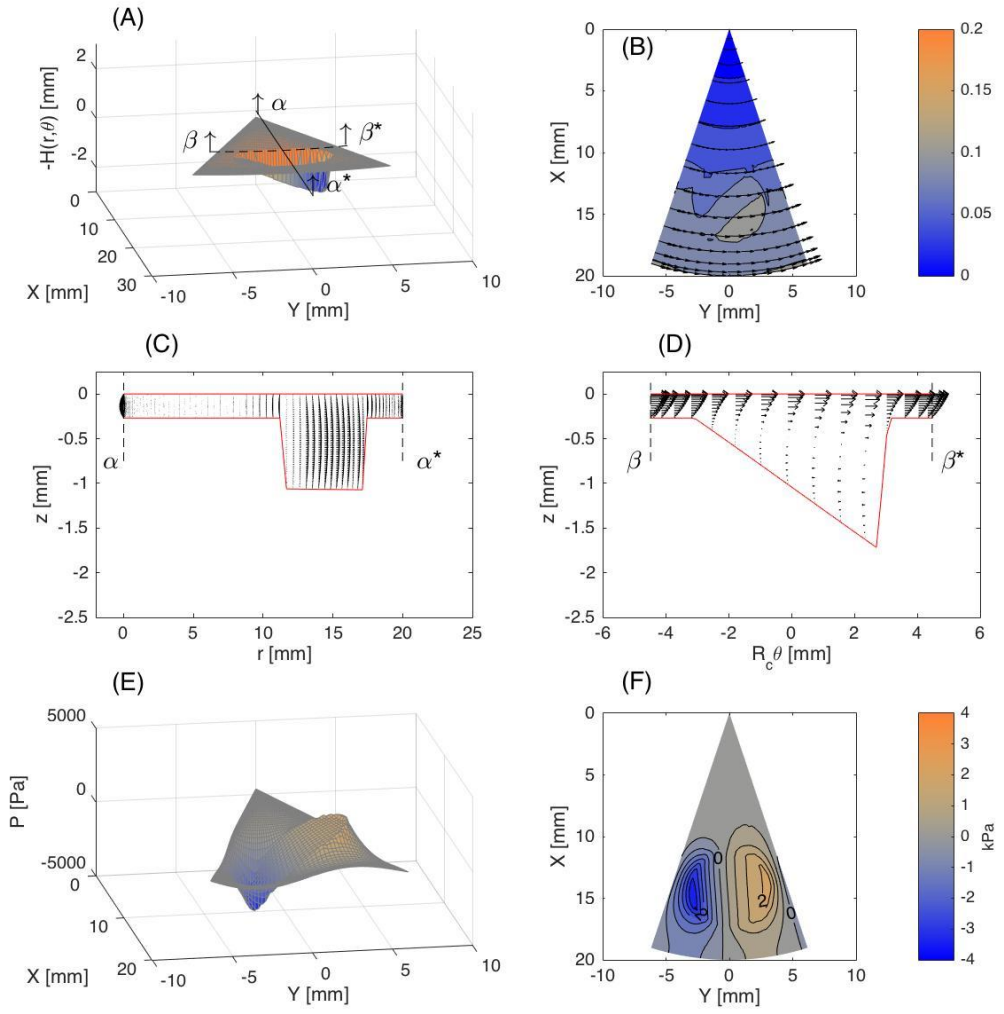

Figure S5: Example computed fields obtained with the Reynolds equation for an asymmetric surface texture with β=14° and Ω=10 rad/s at h_0=269 μm, which fall within the regions of applicability given in Figure 7. These computed fields were obtained for each texture tested with input values given in Table 2. (A) surface texture profile, plotted as -h. (B) plot of the velocity field at $z=h_0/2$. (C) velocity field of v_r and v_z at θ=0°. (D) velocity field of v_θ and v_z at $r=R_t$. (E) computed pressure profile. (F) contour of pressure.

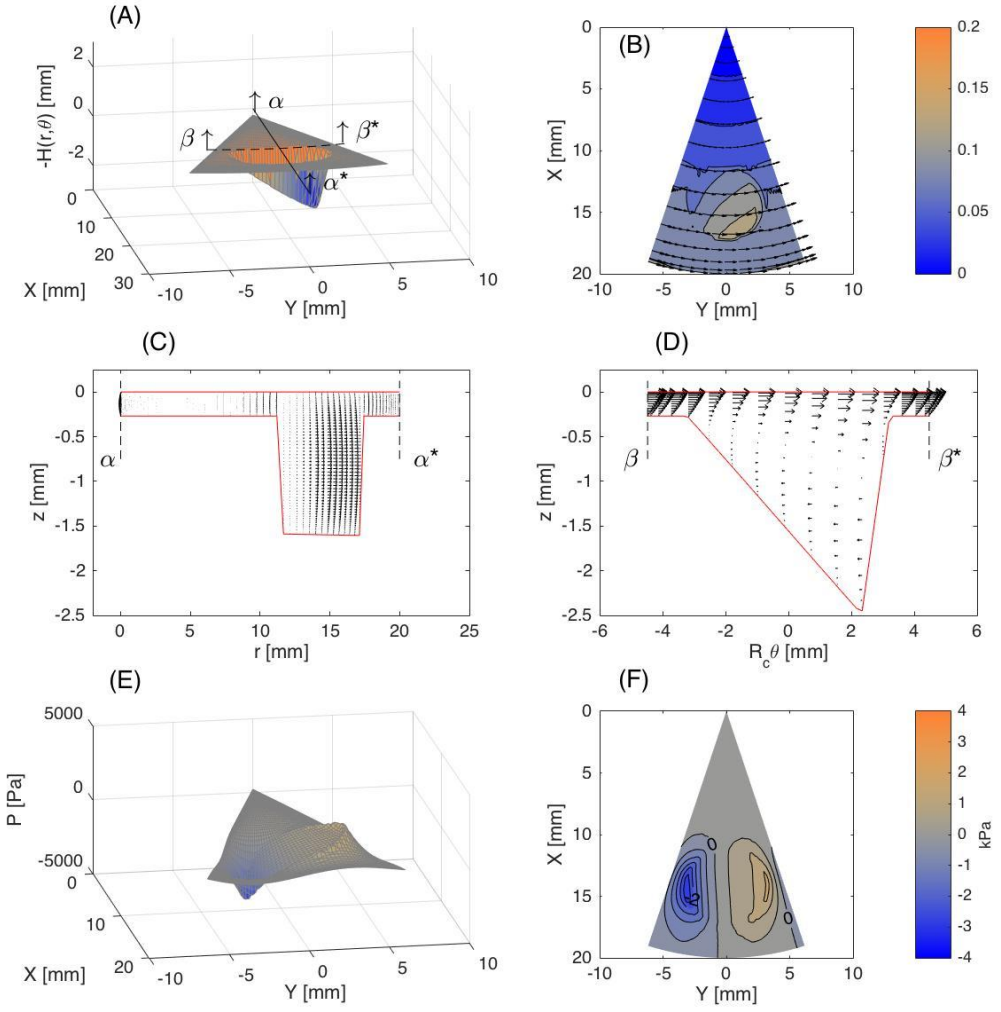

Figure S6: Example computed fields obtained with the Reynolds equation for an asymmetric surface texture with β=21.7° and Ω=10 rad/s at h_0=269 μm, which fall outside the regions of applicability given in Figure 7. These computed fields were obtained for each texture tested with input values given in Table 2. (A) surface texture profile, plotted as -h. (B) plot of the velocity field at $z=h_0/2$. (C) velocity field of v_r and v_z at θ=0°. (D) velocity field of v_θ and v_z at $r=R_t$. (E) computed pressure profile. (F) contour of pressure.

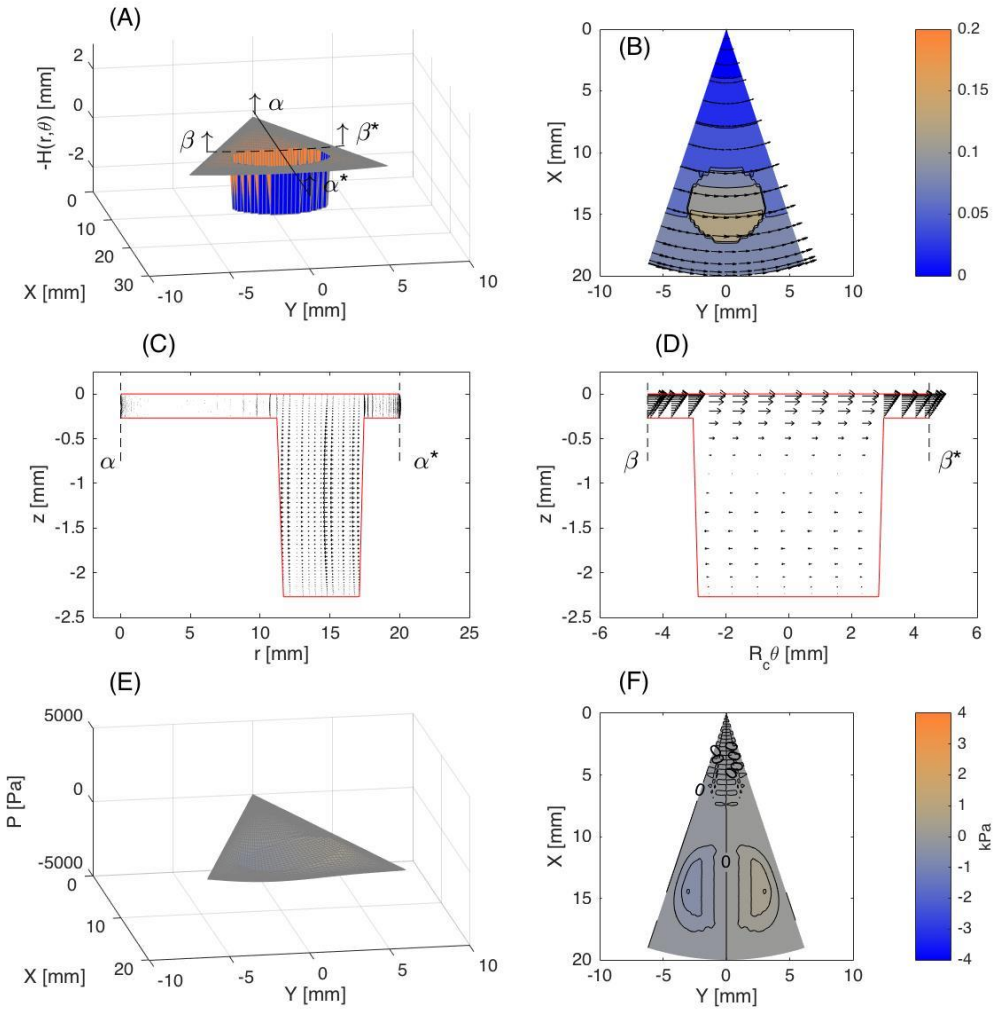

Figure S7: Example computed fields obtained with the Reynolds equation for a symmetric surface texture with D=2 mm and Ω=10 rad/s at h_0=269 μm, which fall outside the regions of applicability given in Figure 7. These computed fields were obtained for each texture tested with input values given in Table 2. (A) surface texture profile, plotted as -h. (B) plot of the velocity field at $z=h_0/2$. (C) velocity field of v_r and v_z at θ=0°. (D) velocity field of v_θ and v_z at $r=R_t$. (E) computed pressure profile. (F) contour of pressure.

Figure S8 shows the fully textured disk with β=5.3°, similar to those tested experimentally. Figure S9 shows the pressure profile for the fully textured disk with β=5.3°; the maximum value of the pressure is seen at the texture locations, and the pressure is periodic. Figure S10 shows the

shear stress at the moving surface for a fully textured disk with β=5.3°; the shear stress inside the textured region is lower than in the surrounding non-textured region, resulting in an effectively smaller sliding force on the moving surface.

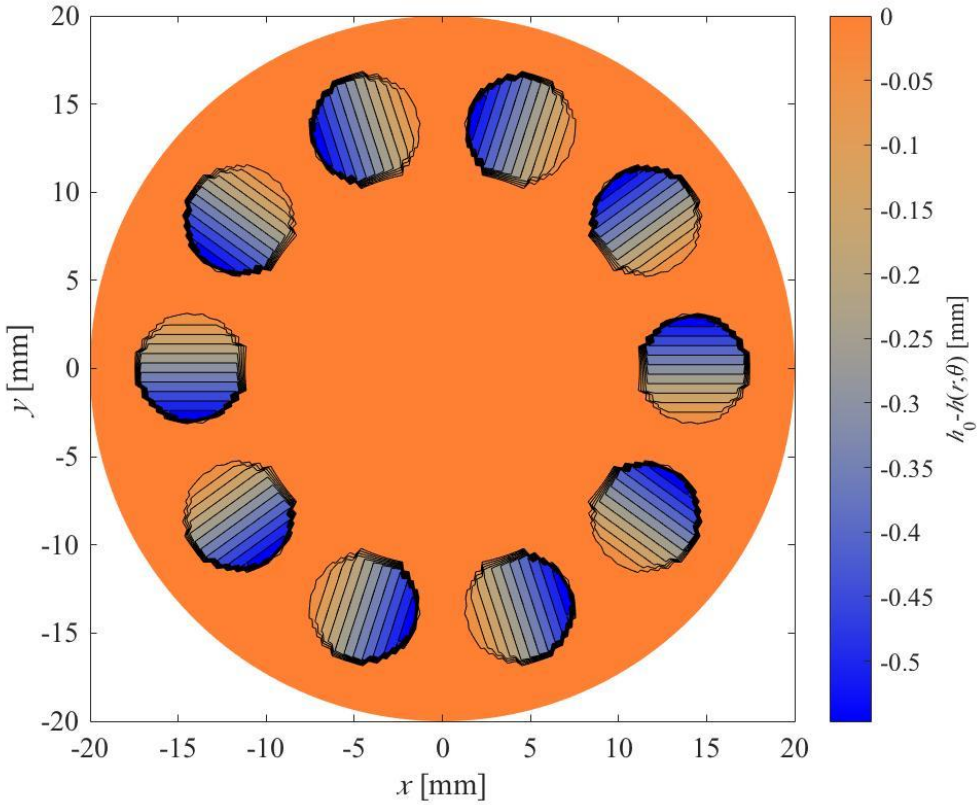

Figure S8: Fully textured disk profile with asymmetric angle β=5.3°. The textured surface is periodic, and matches experimentally tested disks.

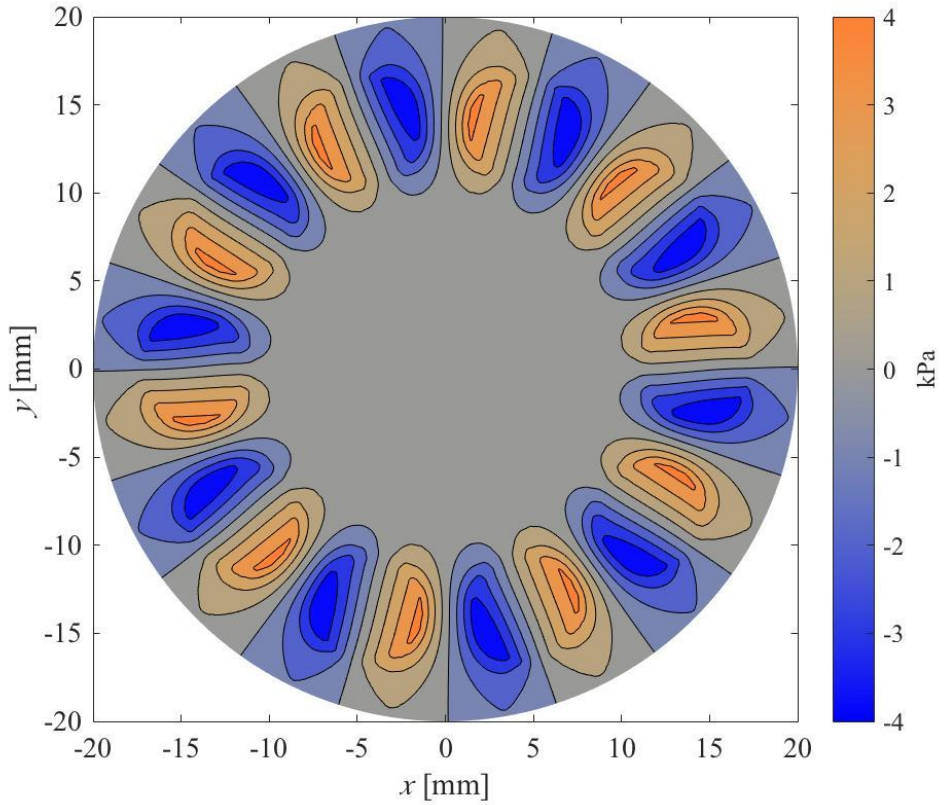

Figure S9: Pressure profile for fully textured surface with asymmetric angle β=5.3°. The pressure profile is periodic, and the maximum value of the pressure occurs at the location of the surface textures.

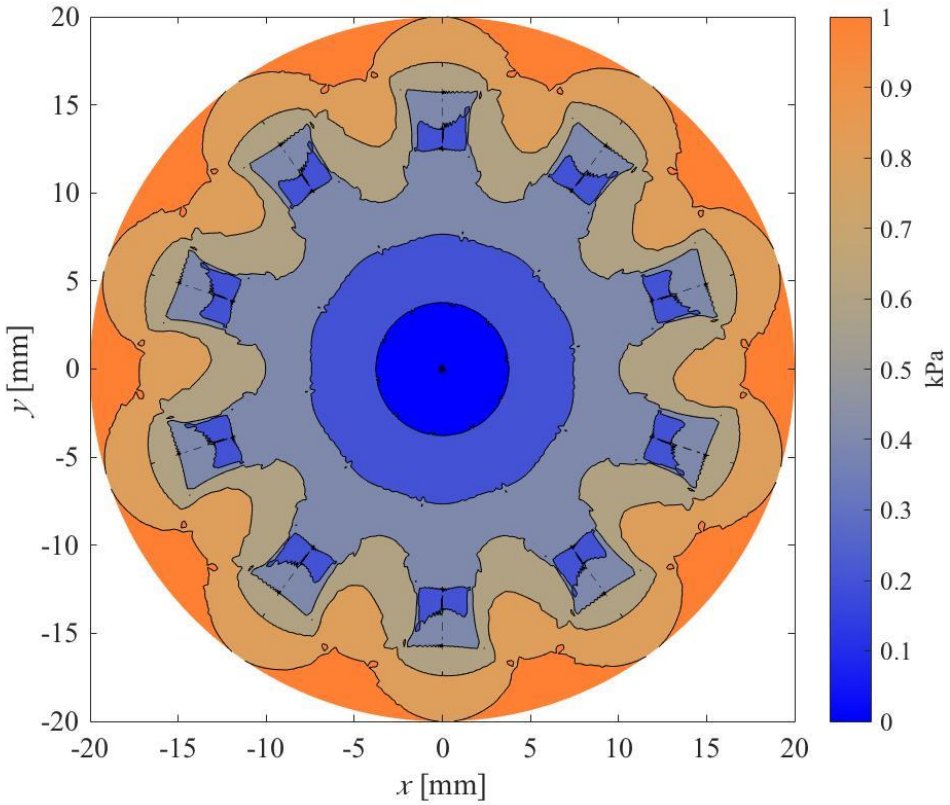

Figure S10: Shear stress profile for fully textured surface with asymmetric angle β=5.3° at the moving flat surface. The shear stress profile is periodic, and the shear stress is lowered inside the textured region (compared to that of a flat disk), effectively decreasing the sliding force on the moving plate.

Figure S11 shows the numerical torque obtained as a function of angular velocity Ω for different angles of asymmetry β at a given gap height h_0=269 μm. A monotonic trend is seen that when β is increased, the torque for a given Ω decreases, and the smallest torque value occurs at the largest β.

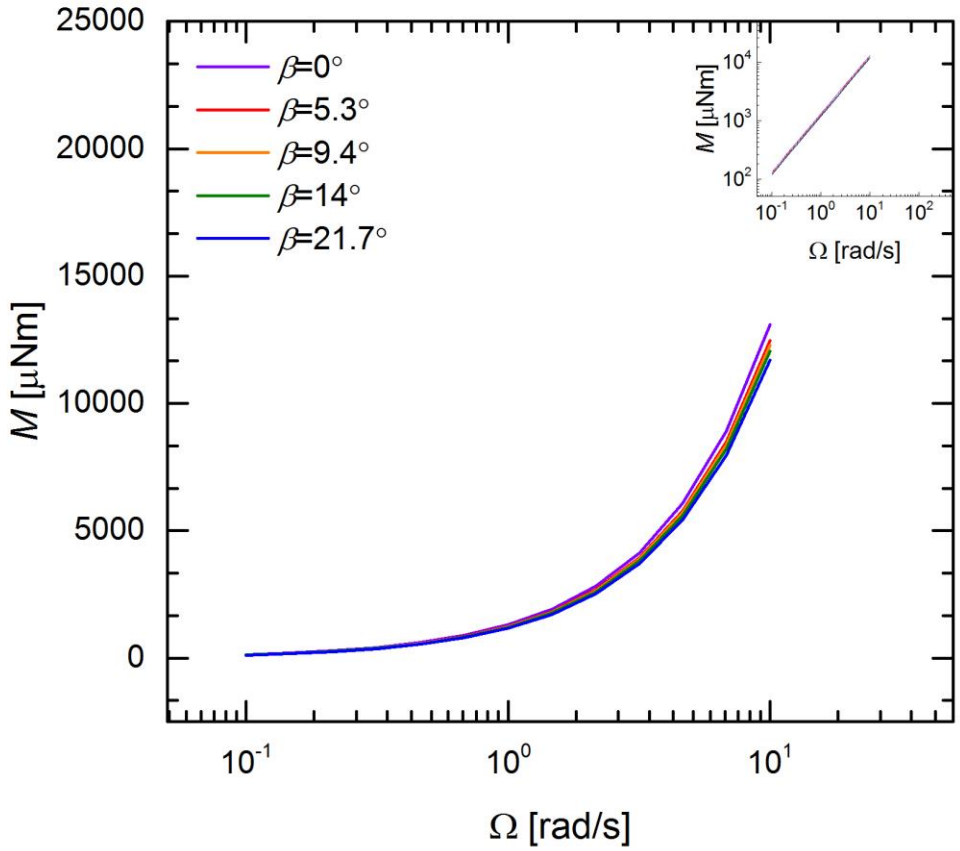

Figure S11: Numerical torque values obtain from simulations at different angular velocities Ω for different angles of asymmetry β. The results show a monotonic trend that increasing β decreases the torque measured at a given Ω.

Figure S12 shows numerical normal force values obtained as a function of angular velocity Ω for different angles of asymmetry β at a given gap height h_0=269 μm. A non-monotonic trend is observed where increasing β from 0° to 5.3° causes an increase in the normal force for a given Ω, but when β increases beyond 5.3°, the normal force decreases for a given Ω.

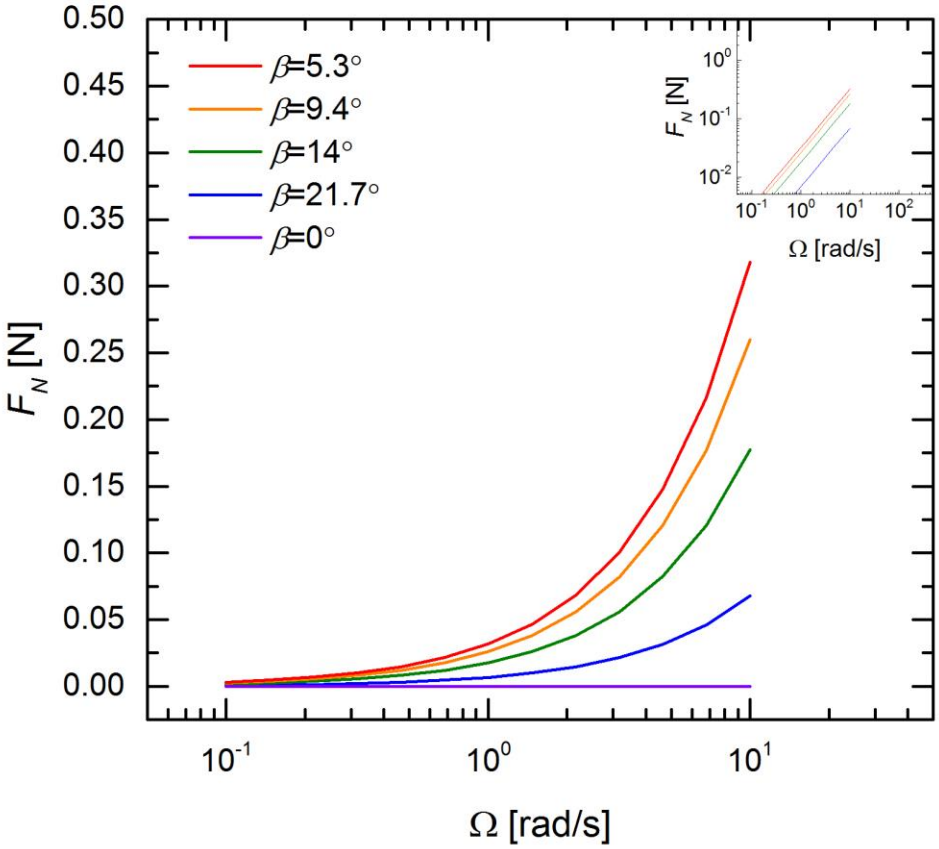

Figure S12: Numerical normal force values obtain from simulations at different angular velocities Ω for different angles of asymmetry β. The results show a non-monotonic trend where increasing β increases the normal force at a given Ω between β=0° and β=5.3°, but for β>5.3° the normal force decreases as β increases.

Figure S13 shows numerical friction coefficient values obtained as a function of angular velocity Ω for different angles of asymmetry β at a given gap height h_0=269 μm. A non-monotonic trend is observed where increasing β from 0° to 5.3° causes a decrease in the friction coefficient (independent of Ω), but when β increases beyond 5.3°, the friction coefficient increases (independent of Ω). The independence with respect to angular velocity occurs because both the torque and normal force depend linearly on Ω, which cancels out when taking the ratio use to define the friction coefficient.

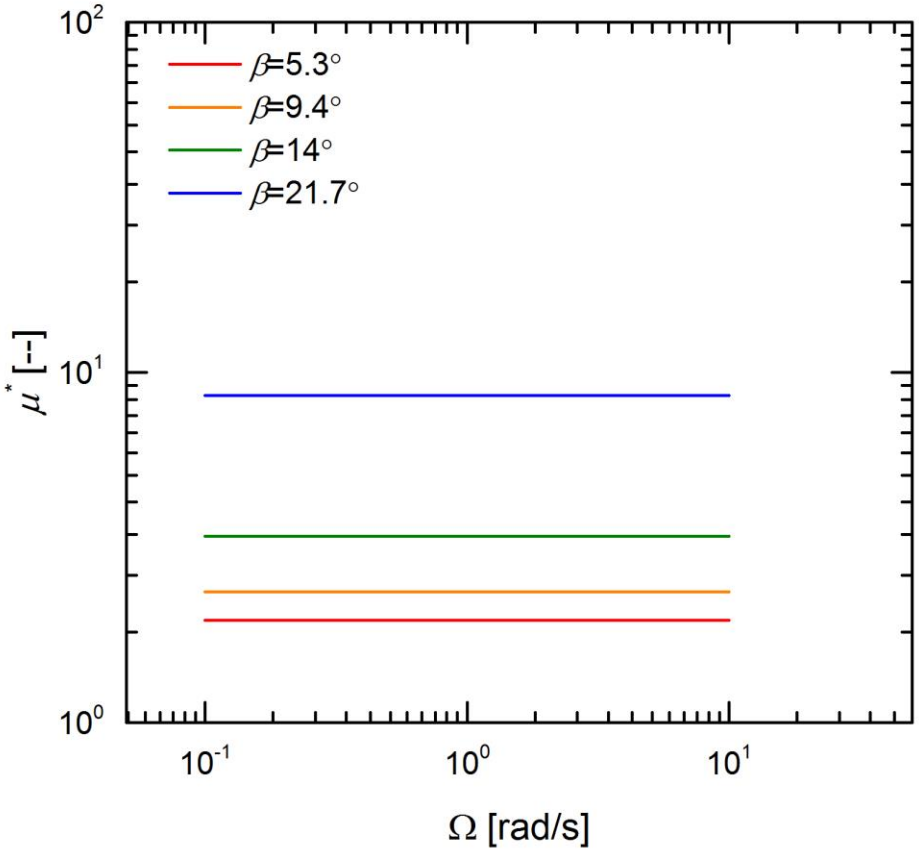

Figure S13: Numerical friction coefficient (ratio of shear and normal load) obtained from simulations at different angular velocities Ω for different angles of asymmetry β. The results show a non-monotonic trend where increasing β decreases the friction coefficient (independent of Ω) between β=0° and β=5.3°, but after this point the friction coefficient increases as β increases (independent of Ω). The friction coefficient is independent of velocity since pressure and stresses all scale linearly with velocity for this low Reynolds number viscous flow (without cavitation).

References

[1] K. E. Beschorner, C. F. Higgs III and M. R. Lovell, "Derivation of Reynolds equation in cylindrical coordinates applicable to pin-on-disk and cmp," in *Proceedings of the STLE/ASME International Joint Tribology Conference*, Miami, FL, USA, 2008.

[2] M. Heath, Scientific Computing: An Introductory Survey, 2nd Edition ed., McGraw-Hill, 2002.

[3] A. Ronen, I. Etsion and Y. Kligerman, "Friction-reducing surface-texturing in reciprocating automotive components," *Tribology Transactions,* vol. 44, no. 3, pp. 359-366, 2001.

[4] R. Siripuram and L. Stephens, "Effect of deterministic asperity geometry on hydrodynamic lubrication," *Journal of Tribology,* vol. 126, pp. 527-534, 2004.

[5] Y. Qiu and M. Khonsari, "On the prediction of cavitation in dimples using a mass-conservative algorithm," *Journal of Tribology,* vol. 131, pp. 041702-1-11, 2009.

[6] S. Kango, D. Singh and R. Sharma, "Numerical investigation on the influence of surface texture on the performance of hydrodynamic journal bearing," *Meccanica,* vol. 47, pp. 469-482, 2012.

[7] N. Tala-Ighil, P. Maspeyrot, M. Fillon and A. Bountif, "Effects of surface texture on journal-bearing characteristics under steady-state operating conditions," *Proceedings of the Institution of Mechanical Engineers, Part J: Journal of Engineering Tribolgoy,* vol. 221, pp. 623-633, 2007.

[8] L. Wang, W. Wang, H. Wang, T. Ma and Y. Hu, "Numerical analysis on the factors affecting the hydrodynamic performance for the parallel surfaces with microtextures," *Journal of Tribology,* vol. 136, pp. 021702-1-8, 2014.

[9] H. Yu, X. Wang and F. Zhou, "Geometric shape effects of surface texture on the generation of hydrodynamic pressure between conformal contacting surfaces," *Tribology Letters,* vol. 37, pp. 123-130, 2010.

[10] Y. Feldman, Y. Kligerman, I. Etsion and S. Haber, "The validity of the Reynolds equation in modeling hydrostatic effects in gas lubricated textured parallel surfaces," *Journal of Tribology,* vol. 128, pp. 345-350, 2006.

[11] M. Qiu, B. Bailey, R. Stoll and B. Raeymaekers, "The accuracy of the compressible Reynolds equation for prediction the local pressure in gas-lubricated textured parallel slider bearing," *Tribology International,* vol. 72, pp. 83-89, 2014.

[12] T. Woloszynski, P. Podsiadlo and G. Stachowiak, "Evaluation of discretization and integration methods for the analysis of hydrodynamic bearings with and without surface texturing," *Tribology Letters,* vol. 51, pp. 25-47, 2013.

[13] M. Dobrica and M. Fillon, "About the validity of Reynolds equation and inertia effects in textured sliders of infinite width," *Proceedings of the Institution of Mechanical Engineers, Part J: Journal of Engineering Tribology,* vol. 223, pp. 69-78, 2009.

[14] J. Ferziger and M. Peric, Computational Methods for Fluid Dynamics, vol. 3, Springer, 2002.

[15] G. Jang, S. Lee and H. Kim, "Finite element analysis of the coupled journal and thrust bearing in a computer hard disk drive," *Journal of Tribology,* vol. 128, pp. 335-340, 2006.

[16] M. E. Wahl and F. E. Talke, "Numerical simulation of the steady state flying characteristics of a 50% slider with surface texture," *IEEE Transactions on Magnetics,* vol. 30, pp. 4122-4124, 1994.

[17] G. Karniadakis and S. Sherwin, Spectral/hp Element Methods for Computational Fluid Dynamics, Oxford University Press, 2005.

[18] M. Schumack, "Application of the psuedospectral method to thermohydrodynamic lubrication," *International Journal for Numerical Methods in Fluids,* vol. 23, pp. 1145-1161, 1996.

[19] S. Gantasala, I. R. P. Krishna and A. S. Sekhar, "Dynamic analysis of rotors supported on journal bearings by solving Reynolds equation using pseudospectral method," in *Proceedings of the 9th IFToMM International Conference on Rotor Dynamics*, 2015.

[20] D. Kopriva, Implementing Spectral Methods for Partial Differential Equations, Springer, 2009.

[21] M. Hussaini and T. Zang, "Spectral methods in fluid dynamics," *Annual Review of Fluid Mechancis*, vol. 19, pp. 339-367, 1987.

[22] B. Fornberg and D. Sloan, "A review of pseudo spectral methods for solving partial differential equations," *Acta Numerica*, vol. 3, pp. 203-267, 1994.

[23] J. Shen, "Efficient spectral-galerkin method I. Direct solvers of second- and fourth-order euqations using Legendre polynomials," *SIAM Journal of Scientific Computing*, vol. 15, pp. 1489-1505, 1994.

[24] Y. Lee, J. Schuh, R. Ewoldt and J. Allison, "Shape parameterization comparison for full-film lubrication texture design," in *ASME 2016 International Design Engineering Technical Conferences, to appear*, Charlotte, NC, USA, 2016.

[25] B. Fornberg, A Practical Guide to Pseudospectral Methods, Cambridge: Cambridge University Press, 1998.

[26] M. Deville, P. Fischer and E. Mund, High-Order Methods for Incompressible Fluid Flow, Cambridge University Press, 2002.

[27] G. Strang, Computational Science and Engineering, Wellesley-Cambridge, 2007.

[28] L. Meirovitch, Fundamental of Vibrations, Waveland Press, Inc., 2010.

[29] J. Schuh and R. Ewoldt, "Asymmetric surface textures decrease friction with Newtonian fluids in full film lubricated sliding contact," *Tribology International*, vol. 97, pp. 490-498, 2016.

[30] M. Qiu, B. Bailey, R. Stoll and B. Raeymakers, "The accuracy of the compressible Reynolds equation for prediction the local pressure in gas-lubricated textured parallel slider bearing," *Tribology International*, vol. 72, pp. 83-89, 2014.